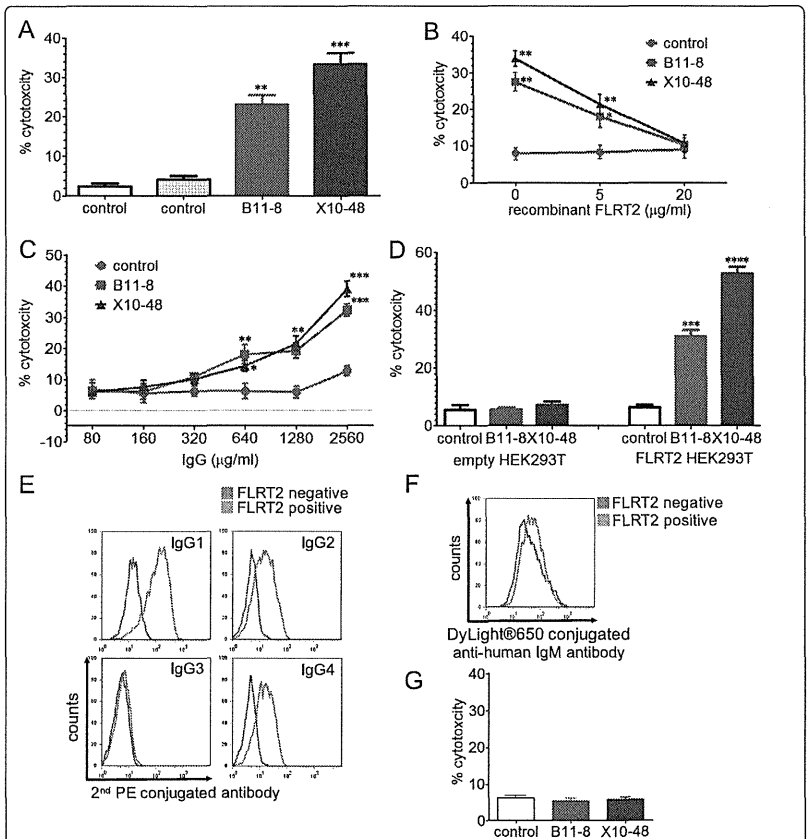

Figure 6 Complement-dependent cytotoxicity (CDC) of anti-FLRT2 antibody. CDC activities using two healthy control IgG and two anti-FLRT2 positive IgG, B11-8 and X10-48, at a concentration of 1.28 mg/ml with 1:3 diluted complement **(A)**, 1.28 mg/ml of IgG, and 1:3 diluted complement with recombinant FLRT2 at the indicated concentrations **(B)**, and various IgG concentrations with 1:6 diluted complement **(C)** against HUVECs were measured with the WST-1 assay. **(D)** CDC activities against mock transfected HEK293T cells (empty, left) and FLRT2-expressing HEK293T cells (FLRT2, right) by using 1.28 mg/ml of IgG and 1:3 diluted complement were measured with the WST-1 assay. HEK293T cells negative or positive for FLRT2 expression were stained with anti-FLRT2 antibody followed by secondary antibody against human IgG1, IgG2, IgG3, IgG4 **(E)**, and IgM **(F)**, and analyzed with flow cytometry. **(G)** ADCC activities using control IgG, B11-8, and X10-48, at a concentration of 1.28 mg/ml with an E:T ratio of 25:1 were determined with the lactate dehydrogenase detection method. Error bars indicate SD. $^{*}P < 0.05$; $^{**}P < 0.01$; $^{***}P < 0.001$; $^{****}P < 0.0001$.

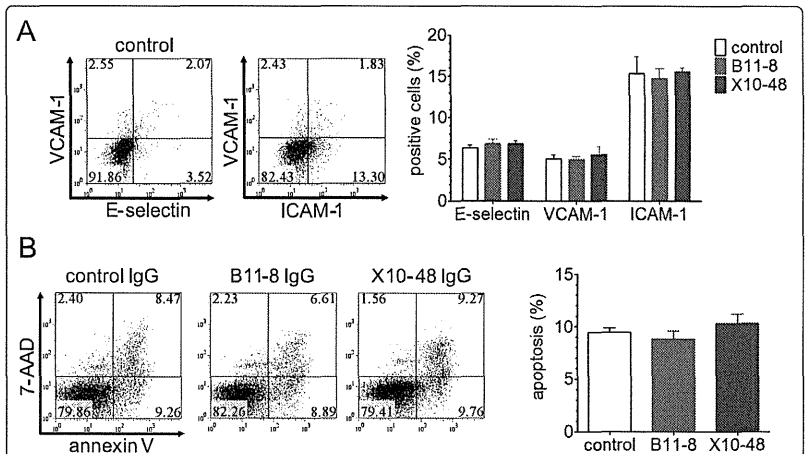

Figure 7 Activation of HUVECs and induction of apoptosis. (A) Expression of E-selectin, intercellular adhesion molecule 1 (ICAM-1), and vascular cell adhesion molecule 1 (VCAM-1) was analyzed with flow cytometry against HUVECs treated with 640 μg/ml of control and two anti-FLRT2-positive IgGs, B11-8 and X10-48. Representative graphs (left) and summarized graph (right) are shown. **(B)** HUVECs treated with control IgG and two anti-FLRT2-positive IgGs, B11-8 and X10-48, for 24 hours were stained with annexin V and 7-AAD and analyzed with flow cytometry. (Annexin V positive/7-AAD negative) cells were measured as apoptotic cells. Representative graphs (left) and summarized graph (right) are shown. Error bars indicate SD.

an important factor for its pathogenicity *in vivo*, in terms of accessibility of the target molecule to AECAs.

Our strategy to identify AECA target molecules is to use a retroviral vector system and flow cytometry. As the localization of cellular molecules depends on their structures, only cell-surface molecules are expressed on the surface of YB2/0 cells transfected with the HUVEC cDNA library. AECAs can bind only to cell-surface molecules in flow cytometry. Therefore, sorting of IgG-binding cells can concentrate and isolate cells expressing autoantigens (target molecules for AECAs) on the cell surface. Although this system may present difficulties in sorting cells at very low frequency, we isolated and cloned autoantigen-expressing cells by repeated sorting, and this system was shown to be useful to identify cell-surface autoantigens. Whereas some cell-surface molecules were identified with this system previously [39], this is the first report of autoantigen identification.

With purified IgG from one SLE patient with high AECA activity (E10-19), two distinct clones were isolated and established, both of which were shown to have an identical gene, *FLRT2*. As we confirmed that E10-19 IgG bound specifically to cell-surface FLRT2 and FLRT2 was expressed on the cell surface of ECs, we concluded that FLRT2 is a novel cell-surface autoantigen as a target molecule for AECAs in SLE patients.

Analysis of anti-FLRT2 activity among patients with various collagen diseases indicated that anti-FLRT2 antibody was specifically detected in SLE, and it accounted for 21.4% of cell-surface target molecules of AECAs in SLE. AECA activity of IgG from SLE patients with anti-FLRT2 activity was significantly inhibited by soluble recombinant FLRT2, indicating that FLRT2 is the major target on ECs for AECAs in these patients. Although heat-shock protein 60 (Hsp60) has been described as the target antigen of AECAs in SLE and has a proapoptotic effect [40,41], Hsp60 was not detected on freshly isolated unstressed HUVECs [40,41]. The remaining 78.6% of SLE patients with AECA activity in the present study may have other as-yet-unidentified target antigens.

FLRT2 is transmembrane protein and was identified as a novel gene family in the screening for extracellular matrix proteins expressed in muscle [38]. Although FLRT2 was shown to be expressed in the pancreas, skeletal muscle, brain, and heart with Northern blotting [38], we confirmed the expression of FLRT2 on HUVECs and other ECs (HAECs, HRGECs, and HMVEC-Ls), and treatment with neither tumor necrosis factor-α (TNF-α)

nor lipopolysaccharide (LPS) induced the expression of FLRT2 (data not shown). E10-19 IgG did not bind to FLRT1 and FLRT3, and these two molecules were not expressed on ECs. Consistent with these findings, the major epitope for anti-FLRT2 antibody was localized in the unique region within the extracellular domain of FLRT2.

FLRT2 has been reported to modulate signaling, interact with fibroblast growth factor receptor, promote cell proliferation, participate in craniofacial development, and promote heart morphogenesis [42-46]. Although we hypothesized that anti-FLRT2 antibody may affect some cellular behavior and induce expression of adhesion molecules, cell proliferation, and apoptotic cell death without complement in ECs, we did not find these activities in the present study.

Among SLE patients with anti-FLRT2 activity, complement levels were correlated significantly with the anti-FLRT2 antibody titer. Moreover, anti-FLRT2 antibody induced cell damage in a complement-dependent manner, suggesting that it has pathogenic roles in immune-mediated vascular damage. CDC activity of AECAs was reported in patients with SLE, Takayasu arteritis, hemolytic-uremic syndrome, and Kawasaki disease [2,4,35,47,48]. Although ADCC activity was not proven in our study, similar observations of AECAs producing CDC but not ADCC were reported previously [35,48].

As demonstrated in this study, FLRT2 is widely distributed in various types of ECs. Therefore, it is possible that anti-FLRT2 antibody is linked to systemic vascular injury. These observations indicate that it is necessary to evaluate the contributions of anti-FLRT2 antibody to atherosclerotic lesions because chronic inflammation is atherogenic in SLE [49,50]. Administration of gammaglobulin was reported to reduce CDC of AECAs against ECs [35], and this may apply to anti-FLRT2 antibody-induced damage. Furthermore, incubation with soluble recombinant FLRT2 inhibited the AECA activity and CDC activity in patients with anti-FLRT2 positivity, which suggests that neutralizing anti-FLRT2 antibodies might be the specific therapeutic approach.

Conclusions

We identified the membrane protein FLRT2 as a novel autoantigen of AECAs in SLE patients. Our retroviral vector system is useful for identification of cell-surface autoantigens. In addition to further investigations of the biologic significance of anti-FLRT2 antibody and its therapeutic applications, other cell-surface autoantigens of AECAs should be determined to achieve a comprehensive understanding of AECA-mediated vascular injury and the development of more-specific intervention strategies.

Abbreviations

ADCC: antibody-dependent cell-mediated cytotoxicity; AECAs: anti-endothelial cell antibodies; APC: allophycocyanin; AUs: arbitrary units; CDC: complement-dependent cytotoxicity; DMEM: Dulbecco modified Eagle medium; ECs: endothelial cells; FBS: fetal bovine serum; FITC: fluorescein isothiocyanate; FLRT: fibronectin leucine-rich transmembrane protein; HAECs: human aortic endothelial cells; HMVEC-Ls: human lung microvascular endothelial cells; HRGECs: human renal glomerular endothelial cells; Hsp60: heat shock protein 60; HUVECs: human umbilical vein endothelial cells; ICAM-1: intercellular adhesion molecule 1; LPS: lipopolysaccharide; MFI: mean fluorescence intensity; PBS: phosphate-buffered saline; PCR: polymerase chain reaction; PE: phycoerythrin; RFUs: relative fluorescence units; SAA: serum amyloid A; SD: standard deviations; SDS: sodium dodecyl sulfate; SLE: systemic lupus erythematosus; SLEDAI: SLE disease activity index; TNF-α: tumor necrosis factor α; VCAM-1: vascular cell adhesion molecule 1; 7-AAD: 7-amino-actinomycin D.

Acknowledgements

We thank the staff of the Department of Hematology and Rheumatology, Tohoku University, for help and discussion, and Reika Saito for technical assistance. We also thank Prof. Masato Nose for critical reading of the manuscript. This work was supported in part by the Network Medicine Global-COE Program from the Ministry of Education, Culture, Sports, Science, and Technology of Japan, and Biomedical Research Core of Tohoku University Graduate School of Medicine.

Author details

[1]Department of Hematology and Rheumatology, Tohoku University Graduate School of Medicine, 1-1 Seiryo-cho, Aoba-ku, Sendai, Miyagi 980-8574, Japan. [2]Department of Histopathology, Tohoku University Graduate School of Medicine, 1-1 Seiryo-cho, Aoba-ku, Sendai, Miyagi 980-8574, Japan.

Authors' contributions

TS and HF carried out the molecular biologic studies, flow cytometry, clinical evaluation, and functional assays and drafted the manuscript. MO participated in the design of the study, performed the molecular biologic studies, and helped to draft the manuscript. KN, RW, YT, NT, and TI participated in its design and helped to draft the manuscript. HH conceived of the study, participated in its design and coordination, and helped to draft the manuscript. All authors read and approved the final manuscript.

Competing interests

The authors declare that they have no competing interests.

Received: 9 March 2012 Revised: 1 June 2012 Accepted: 2 July 2012
Published: 2 July 2012

References

1. Lindqvist KJ, Osterland CK: **Human antibodies to vascular endothelium.** *Clin Exp Immunol* 1971; **96**:753-760.
2. Guilpain P, Mouthon L: **Antiendothelial cells autoantibodies in vasculitis-associated systemic diseases.** *Clin Rev Allergy Immunol* 2008, **35**:59-65.
3. D'Cruz DP, Houssiau FA, Ramirez G, Baguley E, McCutcheon J, Vianna J, Haga HJ, Swana GT, Khamashta MA, Taylor JC, Davies DR, Hughes GR: **Antibodies to endothelial cells in systemic lupus erythematosus: a potential marker for nephritis and vasculitis.** *Clin Exp Immunol* 1991, **85**:254-261.
4. Renaudineau Y, Dugué C, Dueymes M, Youinou P: **Antiendothelial cell antibodies in systemic lupus erythematosus.** *Autoimmun Rev* 2002, **1**:365-372.
5. Soltesz P, Bereczki D, Szodoray P, Magyar MT, Der H, Csipo I, Hajas A, Paragh G, Szegedi G, Bodolay E: **Endothelial cell markers reflecting endothelial cell dysfunction in patients with mixed connective tissue disease.** *Arthritis Res Ther* 2010, **12**:R78.
6. Mihai C, Tervaert JW: **Anti-endothelial cell antibodies in systemic sclerosis.** *Ann Rheum Dis* 2010, **69**:319-324.
7. Chauhan SK, Tripathy NK, Nityanand S: **Antigenic targets and pathogenicity of anti-aortic endothelial cell antibodies in Takayasu arteritis.** *Arthritis Rheum* 2006, **54**:2326-2333.
8. Del Papa N, Guidali L, Sironi M, Shoenfeld Y, Mantovani A, Tincani A, Balestrieri G, Radice A, Sinico RA, Meroni PL: **Anti-endothelial cell IgG antibodies from patients with Wegener's granulomatosis bind to human endothelial cells in vitro and induce adhesion molecule expression and cytokine secretion.** *Arthritis Rheum* 1996, **39**:758-766.
9. Ahmed SS, Tan FK, Arnett FC, Jin L, Geng YJ: **Induction of apoptosis and fibrillin 1 expression in human dermal endothelial cells by scleroderma sera containing anti-endothelial cell antibodies.** *Arthritis Rheum* 2006, **54**:2250-2262.
10. Hahn BH: **Targeted therapies in systemic lupus erythematosus: successes, failures and future.** *Ann Rheum Dis* 2011, **70(Suppl 1)**:i64-i66.
11. Bloom O, Cheng KF, He M, Papatheodorou A, Volpe BT, Diamond B, Al-Abed Y: **Generation of a unique small molecule peptidomimetic that neutralizes lupus autoantibody activity.** *Proc Natl Acad Sci USA* 2011, **108**:10255-10259.
12. Youinou P: **New target antigens for anti-endothelial cell antibodies.** *Immunobiology* 2005, **210**:789-797.
13. Naparstek Y, Plotz PH: **The role of autoantibodies in autoimmune disease.** *Annu Rev Immunol* 1993, **11**:79-104.
14. Racanelli V, Prete M, Musaraj G, Dammacco F, Perosa F: **Autoantibodies to intracellular antigens: generation and pathogenetic role.** *Autoimmun Rev* 2011, **10**:503-508.
15. Praprotnik S, Blank M, Meroni PL, Rozman B, Eldor A, Shoenfeld Y: **Classification of anti-endothelial cell antibodies into antibodies against microvascular and macrovascular endothelial cells: the pathogenic and diagnostic implications.** *Arthritis Rheum* 2001, **44**:1484-1494.
16. Karasawa R, Kurokawa MS, Yudoh K, Masuko K, Ozaki S, Kato T: **Peroxiredoxin 2 is a novel autoantigen for anti-endothelial cell antibodies in systemic vasculitis.** *Clin Exp Immunol* 2010, **161**:459-470.
17. Dieudé M, Senécal JL, Raymond Y: **Induction of endothelial cell apoptosis by heat-shock protein 60-reactive antibodies from anti-endothelial cell autoantibody-positive systemic lupus erythematosus patients.** *Arthritis Rheum* 2004, **50**:3221-3231.
18. Kitamura T, Koshino Y, Shibata F, Oki T, Nakajima H, Nosaka T, Kumagai H: **Retrovirus-mediated gene transfer and expression cloning: powerful tools in functional genomics.** *Exp Hematol* 2003, **31**:1007-1014.
19. Tan EM, Cohen AS, Fries JF, Masi AT, McShane DJ, Rothfield NF: **The 1982 revised criteria for the classification of systemic lupus erythematosus.** *Arthritis Rheum* 1982, **25**:1271-1277.
20. Alarcón-Segovia D, Cardiel MH: **Comparison between three diagnostic criteria for mixed connective tissue disease: study of 593 patients.** *J Rheumatol* 1989, **16**:328-334.
21. Vitali C, Bombardieri S, Jonsson R, Moutsopoulos HM, Alexander EL, Carsons SE, Daniels TE, Fox PC, Fox RI, Kassan SS, Pillemer SR, Talal N, Weisman MH: **Classification criteria for Sjögren's syndrome: a revised version of the European criteria proposed by the American-European Consensus Group.** *Ann Rheum Dis* 2002, **61**:554-558.
22. Bohan A, Peter JB: **Polymyositis and dermatomyositis (parts 1 and 2).** *N Engl J Med* 1975, **292**:344-347, 403-407.
23. Subcommittee for Scleroderma Criteria of the American Rheumatism Association Diagnostic and Therapeutic Criteria Committee: **Preliminary criteria for the classification of systemic sclerosis (scleroderma).** *Arthritis Rheum* 1980, **23**:581-590.
24. Aletaha D, Neogi T, Silman AJ, Funovits J, Felson DT, Bingham CO, Birnbaum NS, Burmester GR, Bykerk VP, Cohen MD, Combe B, Costenbader KH, Dougados M, Emery P, Ferraccioli G, Hazes JM, Hobbs K, Huizinga TW, Kavanaugh A, Kay J, Kvien TK, Laing T, Mease P, Ménard HA, Moreland LW, Naden RL, Pincus T, Smolen JS, Stanislawska-Biernat E, Symmons D, Tak PP, Upchurch KS, Vencovský J, Wolfe F, Hawker G: **2010 Rheumatoid arthritis classification criteria: an American College of Rheumatology/European League Against Rheumatism collaborative initiative.** *Arthritis Rheum* 2010, **62**:2569-2581.
25. Miyakis S, Lockshin MD, Atsumi T, Branch DC, Brey RL, Cervera R, Derksen RH, De Groot PG, Koike T, Meroni PL, Reber G, Shoenfeld Y, Tincani A, Vlachoyiannopoulos PG, Krilis SA: **International consensus statement on an update of the classification criteria for definite antiphospholipid syndrome (APS).** *J Thromb Haemost* 2006, **4**:295-306.
26. Lightfoot RW Jr, Michel BA, Bloch DA, Hunder GG, Zvaifler NJ, McShane DJ, Arend WP, Calabrese LH, Leavitt RY, Lie JT, Masi AT, Mills JA, Stevens MB, Wallace SL: **The American College of Rheumatology 1990 criteria for the classification of polyarteritis nodosa.** *Arthritis Rheum* 1990, **33**:1088-1093.
27. Masi AT, Hunder GG, Lie JT, Michel BA, Bloch DA, Arend WP, Calabrese LH, Edworthy SM, Fauci AS, Leavitt RY, Lightfoot RW Jr, McShane DJ, Mills JA, Stevens MB, Wallace SL, Zvaifler NJ: **The American College of Rheumatology 1990 criteria for the classification of Churg-Strauss syndrome (allergic granulomatosis and angiitis).** *Arthritis Rheum* 1990, **33**:1094-1100.
28. Jennette JC, Falk RJ, Andrassy K, Bacon PA, Churg J, Gross WL, Hagen EC, Hoffman GS, Hunder GG, Kallenberg CG, McCluskey RT, Sinico RA, Rees AJ, Van Es LA, Waldherr R, Wiik A: **Nomenclature of systemic vasculitides: proposal of an international consensus conference.** *Arthritis Rheum* 1994, **37**:187-192.
29. Leavitt RY, Fauci AS, Bloch DA, Michel BA, Hunder GG, Arend WP, Calabrese LH, Fries JF, Lie JT, Lightfoot RE Jr, Masi AT, McShane DJ, Mills JA, Stevens MB, Wallace SL, Zvaifler NJ: **The American College of Rheumatology 1990 criteria for the classification of Wegener's granulomatosis.** *Arthritis Rheum* 1990, **33**:1101-1107.
30. Hunder GG, Bloch DA, Michel BA, Stevens MB, Arend WP, Calabrese LH, Edworthy SM, Fauci AS, Leavitt RY, Lie JT, Lightfoot RW Jr, Masi AT, McShane DJ, Mills JA, Wallace SL, Zvaifler NJ: **The American College of Rheumatology 1990 criteria for the classification of giant cell arteritis.** *Arthritis Rheum* 1990, **33**:1122-1128.
31. Arend WP, Michel BA, Bloch DA, Hunder GG, Calabrese LH, Edworthy SM, Fauci AS, Leavitt RY, Lie JT, Lightfoot RW Jr, Masi AT, McShane DJ, Mills JA, Stevens MB, Wallace SL, Zvaifler NJ: **The American College of Rheumatology 1990 criteria for the classification of Takayasu arteritis.** *Arthritis Rheum* 1990, **33**:1129-1134.
32. Tunç R, Uluhan A, Melikoğlu M, Ozyazgan Y, Ozdoğan H, Yazici H: **A reassessment of the International Study Group criteria for the diagnosis (classification) of Behçet's syndrome.** *Clin Exp Rheumatol* 2001, **19(Suppl)**:45-47.
33. Bordron A, Révélen R, D'Arbonneau F, Dueymes M, Renaudineau Y, Jamin C, Youinou P: **Functional heterogeneity of anti-endothelial cell antibodies.** *Clin Exp Immunol* 2001, **124**:492-501.
34. Morita S, Kojima T, Kitamura T: **Plat-E: an efficient and stable system for transient packaging of retroviruses.** *Gene Ther* 2000, **7**:1063-1066.
35. Tripathy NK, Upadhyaya S, Sinha N, Nityanand S: **Complement and cell mediated cytotoxicity by antiendothelial cell antibodies in Takayasu's arteritis.** *J Rheumatol* 2001, **28**:805-808.
36. Idusogie EE, Presta LG, Gazzano-Santoro H, Totpal K, Wong PY, Ultsch M, Meng YG, Mulkerrin MG: **Mapping of the C1q binding site on rituxan, a chimeric antibody with a human IgG1 Fc.** *J Immunol* 2000, **164**:4178-4184.
37. Yamane-Ohnuki N, Kinoshita S, Inoue-Urakubo M, Kusunoki M, Iida S, Nakano R, Wakitani M, Niwa R, Sakurada M, Uchida K, Shitara K, Satoh M: **Establishment of FUT8 knockout Chinese hamster ovary cells: an ideal host cell line for producing completely defucosylated antibodies with enhanced antibody-dependent cellular cytotoxicity.** *Biotechnol Bioeng* 2004, **87**:614-622.
38. Lacy SE, Bönnemann CG, Buzney EA, Kunkel LM: **Identification of FLRT1, FLRT2, and FLRT3: a novel family of transmembrane leucine-rich repeat proteins.** *Genomics* 1999, **62**:417-426.
39. Suzuki J, Umeda M, Sims PJ, Nagata S: **Calcium-dependent phospholipid scrambling by TMEM16F.** *Nature* 2010, **468**:834-838.
40. Alard JE, Dueymes M, Youinou P, Jamin C: **Modulation of endothelial cell damages by anti-Hsp60 autoantibodies in systemic autoimmune diseases.** *Autoimmun Rev* 2007, **6**:438-443.
41. Jamin C, Dugué C, Alard JE, Jousse S, Saraux A, Guillevin L, Pierre JC, Youinou P: **Induction of endothelial cell apoptosis by the binding of anti-endothelial cell antibodies to Hsp60 in vasculitis-associated systemic autoimmune diseases.** *Arthritis Rheum* 2005, **52**:4028-4038.
42. Yamagishi S, Hampel F, Hata K, Del Toro D, Schwark M, Kvachnina E, Bastmeyer M, Yamashita T, Tarabykin V, Klein R, Egea J: **FLRT2 and FLRT3 act as repulsive guidance cues for Unc5-positive neurons.** *EMBO J* 2011, **30**:2920-2933.
43. Wei K, Xu Y, Tse H, Manolson MF, Gong SG: **Mouse FLRT 2 interacts with the extracellular and intracellular regions of FGFR2.** *J Dent Res* 2011, **90**:1234-1239.
44. Xu Y, Wei K, Kulyk W, Gong SG: **FLRT2 promotes cellular proliferation and inhibits cell adhesion during chondrogenesis.** *J Cell Biochem* 2011, **112**:3440-3448.
45. Gong SG, Mai S, Chung K, Wei K: **Flrt2 and Flrt3 have overlapping and non-overlapping expression during craniofacial development.** *Gene Expr Patterns* 2009, **9**:497-502.

46. Müller PS, Schulz R, Maretto S, Costello I, Srinivas S, Bikoff E, Robertson E: **The fibronectin leucine-rich repeat transmembrane protein Flrt2 is required in the epicardium to promote heart morphogenesis.** *Development* 2011, **138**:1297-1308.
47. Leung DY, Moake JL, Havens PL, Kim M, Pober JS: **Lytic anti-endothelial cell antibodies in haemolytic-uraemic syndrome.** *Lancet* 1988, **2**:183-186.
48. Fujieda M, Oishi N, Kurashige T: **Antibodies to endothelial cells in Kawasaki disease lyse endothelial cells without cytokine pretreatment.** *Clin Exp Immunol* 1997, **107**:120-126.
49. Salmon JE, Roman MJ: **Subclinical atherosclerosis in rheumatoid arthritis and systemic lupus erythematosus.** *Am J Med* 2008, **121(Suppl 1)**:3-8.
50. Roman MJ, Shanker BA, Davis A, Lockshin MD, Sammaritano L, Simantov R, Crow MK, Schwartz JE, Paget SA, Devereux RB, Salmon JE: **Prevalence and correlates of accelerated atherosclerosis in systemic lupus erythematosus.** *N Engl J Med* 2003, **349**:2399-2406.

doi:10.1186/ar3897
Cite this article as: Shirai *et al.*: **A novel autoantibody against fibronectin leucine-rich transmembrane protein 2 expressed on the endothelial cell surface identified by retroviral vector system in systemic lupus erythematosus.** *Arthritis Research & Therapy* 2012 **14**:R157.

J. Micromech. Microeng. **22** (2012) 105015 (11pp) doi:10.1088/0960-1317/22/10/105015

Pillar-shaped stimulus electrode array for high-efficiency stimulation of fully implantable epiretinal prosthesis

Kang-Wook Lee[1], Yoshinobu Watanabe[2], Chikashi Kigure[2], Takafumi Fukushima[1], Mitsumasa Koyanagi[1] and Tetsu Tanaka[2]

[1] New Industry Creation Hatchery Center (NICHe), Tohoku University, 6-6-01 Aza-Aoba, Aramaki, Aoba-ku, Sendai 980-8579, Japan
[2] Department of Biomedical Engineering, Tohoku University, 6-6-01 Aza-Aoba, Aramaki, Aoba-ku, Sendai 980-8579, Japan

E-mail: link@lbc.mech.tohoku.ac.jp

Received 15 February 2012, in final form 26 April 2012
Published 28 August 2012
Online at stacks.iop.org/JMM/22/105015

Abstract

We developed a pillar-shaped microelectrode array (MEA) with varying heights for enhancing the spherical conformity of fully implantable epiretinal prosthesis comprising a 3D stacked retinal chip. The fabricated MEA is composed of 100 pillar electrodes with heights ranging from 60 to 80 μm. The Pt-coated Cu pillar electrode with a surface diameter of 70 μm and a height of 75 μm and the Pt planar electrode with a surface diameter of 70 μm have 24.6 and 125 kΩ impedances, respectively, at 1 kHz *in vitro* experiment. The pillar electrode shows lower impedance than the planar electrode because of a larger surface area. However, to avoid cross-talking between pillar electrodes, we developed a sidewall passivation process of the pillar electrode by using the surface tension of polyimide. The impedance of the isolated pillar electrode 116 kΩ at 1 kHz is similar to the impedance of the planar electrode, because they have similar electrode surface areas. The pillar-shaped MEA shows a better spherical conformity.

(Some figures may appear in colour only in the online journal)

1. Introduction

To date, a number of patients suffer from retinal diseases, such as retinitis pigmentosa (RP) and age-related macular degeneration (AMD). However, effective medical treatments for RP and AMD have yet to be established. In addition, it also is observed that the number of blind patients increases rapidly with the aging of society. Therefore, the alternative treatments for these diseases are strongly required. Photoreceptor cells in a retina play an important function in retinal cells by converting the visual information to neural signal.

However, in most cases, RP and AMD result from impairment of the photoreceptor cells that convert light signal to electrical signal in a retina. On the other hand, the other retinal cells, such as bipolar cells, horizontal cells and ganglion cells, remain normal [1, 2]. Accordingly, it will be possible to recover the patient's vision by stimulating the remaining retinal cells. A number of research groups have reported that light perception can be elicited by the electrical stimulation of the remaining retinal cells [3–6]. Recently, many studies have been reported for retinal prostheses in blind patients to restore visual sensation by electrical stimulation using stimulus electrodes [7–21]. Generally, retinal prosthesis has three indispensable components, such as a photodetector, a signal processing circuit and a stimulus current generator with a stimulus electrode array. The photodetector receives an optical signal from the outside and converts it to an electrical signal after which the processing circuits perform image processing, such as edge extraction and motion detection. Then, the stimulus current generator, placed on the surface of the retina, generates appropriate patterns of electrical current. Finally, the stimulus electrode array stimulates the remaining retinal cells. When the remaining retinal cells are activated by the stimulus current, blind patients would perceive a dot

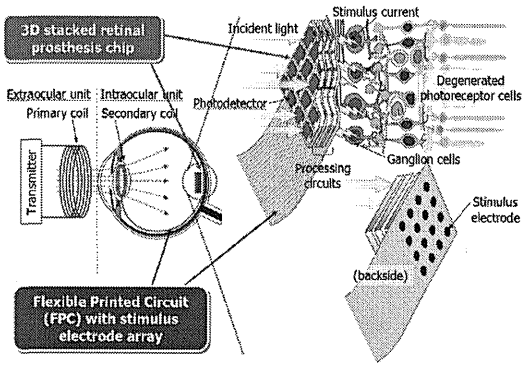

Figure 1. Configuration of fully implantable retinal prosthesis system comprising 3D stacked retinal chip, stimulus current generator with stimulus electrode array and coupling coils.

of light at each stimulation point. In conventional retinal prosthesis, only the stimulus current generator with a few tens of stimulus electrodes is implanted in the eyeball because of a small retinal area of approximately 3 mm^2, which is suitable for retinal chip implantation. Meanwhile, other devices, such as photodetector and processing circuits, are placed outside the eyeball. Therefore, the conventional retinal prosthesis is a large, heavy and complicated system. Moreover, the patients cannot use saccadic effect based on a high-speed eye movement. These disadvantages induce a low quality-of-life (QOL) to the patient. To resolve these issues and to implement similar performance with the human eye, a high-speed, high-performance and small-size artificial retina with saccadic function is required.

To realize such an artificial retina, we have proposed a fully implantable retinal prosthesis system comprising three-dimensional (3D) stacked retinal chip for transforming optical signal to electrical signal and generating stimulus current, microelectrode stimulus array for stimulating retina cells and coupling coils for power transmission as shown in figure 1. This retinal prosthesis can be fully implanted on the surface of the retina, unlike the other group's retinal prosthesis [22]. For realizing a fully implantable retinal prosthesis, we have developed some key components such as a stimulus current generator with a stimulus electrode array and a retinal prosthesis module [22–27].

Figure 2 shows a conceptual cross-sectional structure of 3D stacked retinal chip and stimulus microelectrode array (MEA). The 3D stacked retinal chip comprising photodetectors converts the optical signal received from outside the eyes into an electrical signal, the signal-processing circuits perform image processing, and the stimulus current generator generates appropriate electrical current pattern, bonded on a thin flexible cable with stimulus MEA to stimulate the remaining retinal cells. All component chips are vertically

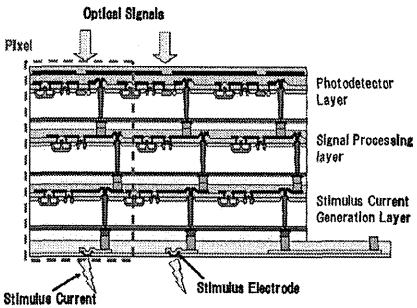

Figure 2. Cross-sectional structure of 3D stacked retinal chip and MEA.

stacked onto one die and electrically connected using high-density, short-length through-silicon vias (TSVs). This leads to a small-sized, light-weight, high fill-factor and high-resolution prosthesis retinal chip. By implanting the 3D stacked retinal chip into an eyeball, patients can employ their own lens and cornea and can rapidly shift a gaze point by moving the eyeball, leading to high-speed visual information processing such as a saccade effect. As the 3D stacked retinal chip has a layered structure similar to the human retina, photodetectors with more than 1000 pixels can be formed in the retinal chip.

To achieve highly efficient stimulation to the retina, it is necessary to establish uniform contact between the retinal cells and the stimulus microelectrodes. However, considering the curvature of the human eyeball, it is hard to make certain contacts to the retinal cells by a planar MEA owing to the distance between them, which is induced by the 3D stacked

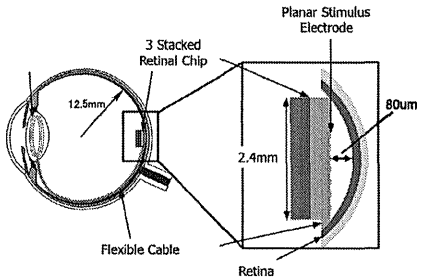

Figure 3. Configuration of fully implantable retinal prosthesis, in which 3D stacked retinal chip was bonded on a flexible cable with the planar-shaped stimulus MEA.

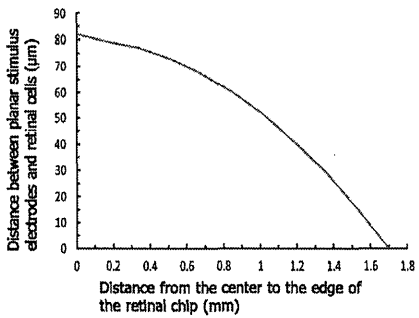

Figure 4. Conceptual relationship of the distance between planar stimulus electrodes and retinal cells in human eye.

retinal chip bonded to a flexible cable with the MEA, as shown in figure 3. We calculated the distance changes with the position from the center to the edge of the planar-shaped stimulus electrodes according to the curvature of the human eyeball by considering that the curvature radius of the human eyeball is 12.5 mm and the area of a 3D stacked artificial retina chip is 2.4 mm^2. There is a maximum distance of 82 μm at the center of the retinal prosthesis chip to the retinal cell in a curved focal plane as shown in figure 4. To achieve a high-resolution retinal prosthesis, it is necessary to stimulate only a target retinal cell. However, this long distance between the planar-shaped stimulus electrodes and the curved focal plane of the human eyeball may induce the low resolution because of a poor stimulation to the retinal cells, because the stimulus current from one stimulus electrode is widespread and stimulates unwanted neighboring retinal cells. This unwanted stimulation may induce tissue damage in neighboring retinal cells. Moreover, the relative distance from its target cell require rise in threshold, and more current will be theoretically necessary for efficient stimulation [28, 29]. It may induce a potential risk to damage the tissue, if the stimulation current level exceeds the level above the non-reversible reactions. To address this problem, penetrating electrodes, which can provide highly specific activation of the targeted neurons [29], have been developed for retinal prosthesis. However, these electrodes, mostly based on the Si technology, have been confirmed to incur acute and chronic damage, and even to lead to degeneration of both the interfaced tissue and the implanted device [30]. Hungar *et al* [31], Wang *et al* [32] and Koo *et al* [33] developed 3D-type flexible MEAs based on parylene and polyimide using Si mold technology for enhancing the spherical conformity of the retinal prosthesis in an eyeball. However, these approaches still have limitations, such as process difficulties and different electrode shapes. In particular, the different arrowhead shapes of electrodes stimulate retina cells differently according to the positions in the array because of the impedance difference at each electrode.

To solve these problems and to achieve highly efficient stimulation to retina cells, we proposed a pillar-shaped stimulus MEA with varying heights, but same surface areas according to the positions in the array using Si micromachining and peel-off processes. The height variation of electrodes allows each electrode to contact the spherical eyeball conformably and approach the stimulus target retinal cells closely. Moreover, the same surface area of electrodes allows stimulating target retinal cells at the same impedance. It can induce enhancement of the spherical conformity of fully implantable retinal prosthesis to the retinal cells in the human eyeball. However, by placing pillar electrodes that intentionally become a flatter surface of the retina chip across the curvature of the eyeball, it has a potential problem of defeating one of the key features of the normal eye, that of the curved focal plane, which does not have aberrations in the image because of differing distances from the lens. However, we assume that this is not as much of a problem, because the distance from the flat retina chip to the curved focal plane is around 80 μm, and it is too short compared with 20 000 μm distance between the lens and the curved focal plane. Moreover, the depth of curvature of the human eyeball is slight, and the retina chip has a tiny area of 2.4 mm^2 and lesser thickness of 100 μm. Therefore, the entire retina chip can be in focus.

In this study, we fabricated the pillar-shaped stimulus MEA with varying heights, but the same surface areas, and characterized the impedance performance of the pillar electrode quantitatively compared with the planar electrode.

2. Design and fabrication of a pillar-shaped stimulus microelectrode

Figure 5 shows the configuration of fully implantable epiretinal prosthesis, in which a 3D stacked retinal chip was bonded to the flexible cable comprising pillar-shaped stimulus electrodes with varying heights. By these pillar electrodes, superior contact can be realized despite the various distances between the 3D stacked retinal chip and the target retinal cells in the spherical eyeball. Therefore, it can improve the stimulation

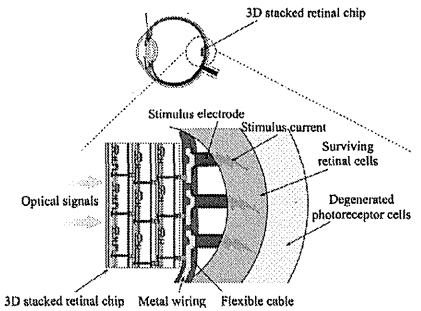

Figure 5. Configuration of fully implantable retinal prosthesis, in which 3D stacked retinal chip was bonded on a flexible cable with the pillar-shape stimulus MEA.

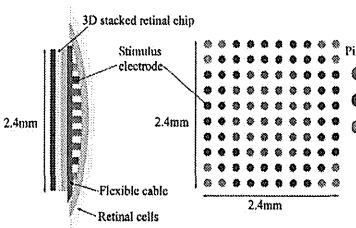

Figure 6. Layout of the pillar stimulus MEA consisting of 100 electrodes with varying heights.

efficiency to the retinal cells and induce highly qualitative resolution of the retinal prosthesis.

To evaluate the effectiveness of pillar electrodes, we proposed a pillar stimulus MEA composed of 100 electrodes, which have different heights of 60–80 μm in accordance with the pillar electrode position in the MEA, as shown in figure 6. The height variation of pillar electrodes allows each electrode to contact target retinal cells of the spherical eyeball conformably despite various distances between the retina chip and the retinal cells. This pillar MEA is formed in the polyimide-based flexible cable, the layout shown in figure 7. The flexible cable is divided into two parts of the retinal prosthesis module for implantation into an eyeball and the connection pad for a power supply. The flexible cable has a length of 35 mm and thickness of 25 μm. An array of 100 pillar stimulus electrodes is formed on the backside of the retinal prosthesis module part (front area) in the flexible cable. The retinal chip is mounted on the front side and electrically connected to stimulus electrodes through Cr/Au wires. The top surface diameter of stimulus pillar electrode is 70 μm, and the pitch between stimulus electrodes is 150 μm. Four holes, which were formed in the flexible cable, were used for

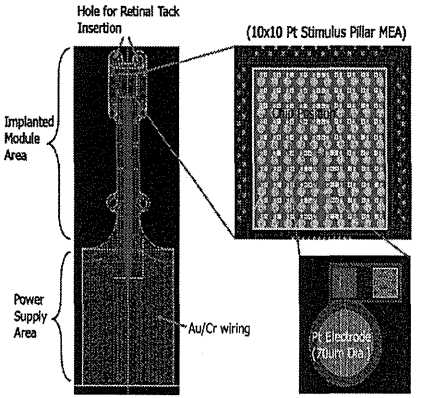

Figure 7. Layout of the flexible cable consisting of 100 Pr stimulus pillar electrodes.

fixation on the retina. Two holes in the edge area were inserted by retinal tacks inside the eyeball, and the other two holes in the middle area were sewn on the sclera outside the eyeball. Figure 8 shows the fabrication process flow of the flexible cable comprising the pillar stimulus MEA with varying heights. First, Si deep via holes with different depths were formed into a Si substrate by changing the cycling steps of plasma SF_6 etching and C_4F_8 passivation in the BOSCH process and using the multiple thickness of the SiO_2 layer. After removing the SiO_2 mask layer, sacrifice layers of sputtered-Al with 100 nm thickness and PECVD-SiO_2 with 200 nm thickness were deposited on the Si substrate and into the holes with the minimum sidewall step coverage of 40% and 60%, respectively. Positive-photosensitive polyimide (CRC 8600, T_g 300 °C) was spin coated on the Si substrate and patterned for the formation of a flexible cable consequently cured for 30 min at 350 °C. The polyimide layer was photo-lithographically patterned not to get down into the pillar holes. The resultant polyimide layer, which is used as a bottom layer of the flexible cable, has a thickness of around 3 μm. After photoresist (PR) patterning for the formation of stimulus electrodes, Pt layer of 100 nm thickness was deposited on the Si surface and into via holes with the minimum sidewall step coverage of 40%. Pt layer and PR layer were removed by a lift-off method using an ultrasonic method except for Pt layer on stimulus electrode areas. However, thin Pt layer of 40 nm thickness in the bottom area of the pillar electrode has the risk of deforming or fracturing during the contact with an eyeball. Therefore, it is necessary to enhance the strength of thin Pt pillar electrode. We proposed to fill Cu material into the pillar holes to improve the strength of the Pt pillar electrode. However, if Cu atoms diffuse to the eyeball passing through the Pt layer, it may induce contamination and consequently damage the retinal cells. To prevent the diffusion of Cu into the eyeball, a sputtered Ta layer of 500 nm thickness was deposed in the Pt pillar holes with

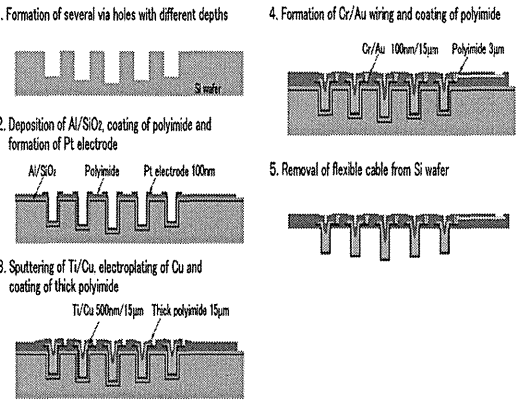

Figure 8. The fabrication process flow of the flexible cable comprising the pillar-shaped stimulus MEA with varying heights.

the minimum sidewall step coverage of 30%. The Ta layer is an attractive film as a Cu barrier because Ta has a high melting point that results in high activation energy for the diffusion process. Then, the Cu seed layer of 500 nm thickness was deposed in the pillar holes with the minimum sidewall step coverage of 40% by sputtering. After PR patterning, the Cu layer of 15 μm thickness was partially filled into the pillar holes using the electroplating process. Thick polyimide was spin coated, patterned and carefully cured for 30 min at 350 °C, with a resultant thickness of 15 μm. This polyimide layer may act as a main frame of the flexible cable and the barrier layer to Cu out-diffusion from the pillar electrode, because it covers the pillar electrodes. The Cr adhesion layer of 100 nm thickness and Au layer of 1 μm thickness were deposited sequentially by the sputtering process and patterned using the wet etching process to make metal wiring for power transmission. A thin polyimide layer (CRC 8600) was spin coated on metal wirings and patterned to open the pads only for power supply. The Au layer is exposed on the pad area and not the Cu layer, because Au may be biocompatible. Finally, the wafer was immersed into the buffered HF solution to etch sacrificial Al and SiO_2 layers and consequently peel-off the flexible cable with pillar-shaped stimulus electrodes from the Si substrate. The Au pad does not affect the HF solution during the peel-off process.

In our process, the formation of via holes with different depths by one-time Si etching process is the key. We utilized the difference of etching rate of Si and SiO_2 in the BOSCH etching process by using multiple thicknesses of SiO_2 hard mask. At first, a 70 nm thick SiO_2 layer was thermally oxidized on a Si substrate. By two-time local patterning and oxide dry etching, SiO_2 hard mask with different thicknesses of 0, 35 and 70 nm was formed on the Si substrate. Via holes with different depths of 60, 70 and 80 μm were fabricated concurrently by the one-time Si BOSCH etching process using multiple thickness SiO_2 hard masks of 70, 35 and 0 nm, respectively, as shown in figure 9. Figure 10 shows the cross-sectional structure of the pillar electrode (*a*) and the photograph of the fabricated pillar electrode (*b*). For enhancing the strength of the Pt pillar electrode, a thick Cu layer of 15 μm thickness was filled well into the pillar holes using the electroplating process. Figure 11 shows the photograph of the fabricated flexible cable with the pillar MEA and the magnified picture of the pillar stimulus electrodes. As shown in the figure, the MEA consisting of 100 stimulus pillar electrodes with different heights ranging from 60 to 80 μm was successfully fabricated.

3. Evaluation of a pillar-shaped stimulus microelectrode

The impedance characteristics of the pillar stimulus electrode–electrolyte interface were evaluated using a Solartron1260 impedance/gain phase analyzer. Measurements were performed within a frequency range from 100 Hz to 100 kHz using 10 mV ac sine signals by immersing the pillar MEA into the 0.9% saline solution. An Ag/AgCl electrode and the pillar electrode were used as a reference electrode along with a counter electrode as shown in figure 12.

To evaluate the impedance characteristics of the pillar electrode, we compared them with the impedance characteristics of a Pt planar electrode with a surface diameter of 70 μm. Figure 13 shows the fabrication process (*a*) and the photograph (*b*) of the flexible cable with the Pt planar electrode array. Positive-photosensitive polyimide (CRC 8600) was spin coated on the Si substrate and patterned for the formation of a flexible cable consequently cured for 30 min at 350 °C. The resultant polyimide layer, which is used as a bottom layer of the flexible cable, has a thickness of around 5 μm. After

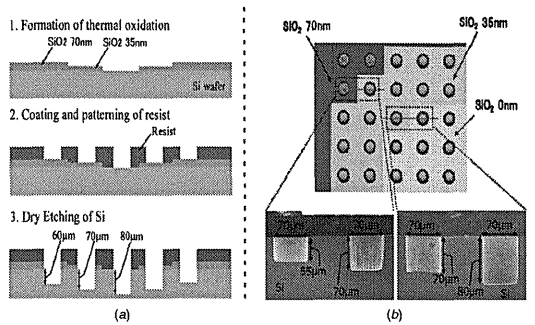

Figure 9. (*a*) The fabrication process flow and (*b*) the photograph of via holes with different heights.

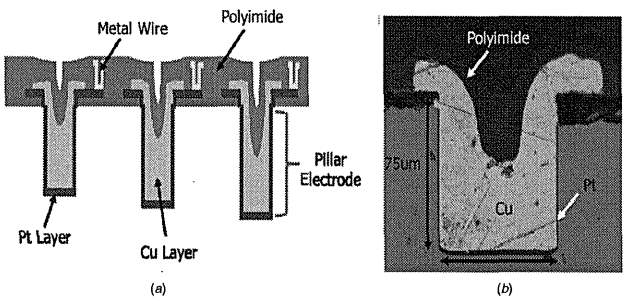

Figure 10. (*a*) Cross-sectional structure of pillar electrodes and (*b*) the photograph of the fabricated pillar electrode.

PR patterning for the formation of a stimulus electrode, the Pt layer of 100 nm thickness was deposited as a stimulus electrode material. The Cr adhesion layer of 100 nm thickness and Au wire of 1 μm thickness were patterned using the sputtering and wet etching processes for the power transmission. Thick polyimide was spin coated, patterned, and carefully cured for 30 min at 350 °C, where it has a resultant thickness of 15 μm. It acts as the main frame of the flexible cable.

Figure 14 shows the impedance characteristics of the pillar electrode and the planar electrode depending on frequencies. The impedances of the pillar and the planar electrodes are 24.6 and 125 kΩ at 1 kHz, respectively. The total surface areas of the pillar electrode (70 μm diameter, 75 μm height) and the planar electrode (70 μm diameter) are theoretically 20 332 and 3846 μm^2. The impedance decrement ratio (1/5.07) of the pillar electrode to the planar electrode is similar, with the difference ratio of the total surface area between them being 5.28. It indicates that the entire surface area of the pillar electrode functions as the stimulus electrode. A large surface area of the pillar electrode reduces the electrode impedance. Therefore, the pillar electrode with lower impedance could contribute to reduce the amount of damage from the stimulation of the retinal cells because of lower charge density [29].

However, the pillar electrode has the risk that it stimulates only a target retinal cell, because of a cross-talking with neighboring electrodes and, consequently, unwanted stimulation around the retinal cells, because the entire surface of the pillar electrode would function as shown in figure 15. To solve this potential problem, we developed a sidewall passivation process of the pillar electrode by using the liquid surface tension as shown in figure 16. The resist block area was formed surrounding the pillar MEA area by PR patterning. The polyimide material (CRC 8600) of 3 μL controlled volume was poured carefully into the edge area of the photoresist mold. Then, the polyimide material was spread into the MEA area and coated on the sidewalls of the pillar electrodes by using liquid surface tension except for the top areas of the electrodes to contact the target retinal cells. If the volume is too large, it would coat the top of the pillars as well. To make the clear surface of the pillar electrode, a plasma-cleaning process known as descumming that use O_2 reactive ion etch,

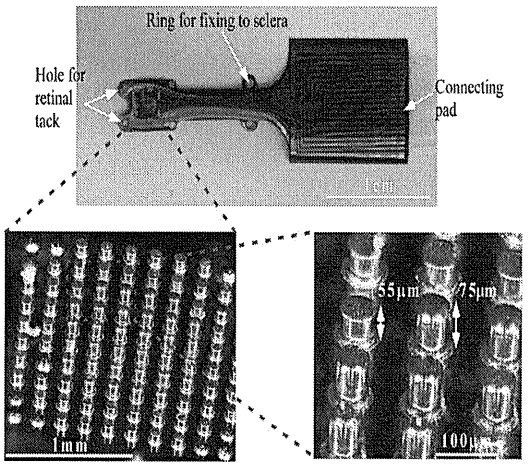

Figure 11. Photographs of the flexible cable comprising 100 stimulus pillar electrodes with different heights.

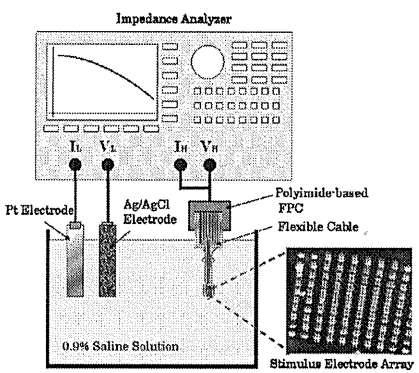

Figure 12. The setup for the three-point impedance measurement.

was lightly applied for 30 s. Figure 17 shows the photographs of the pillar electrode array in which the sidewalls of the pillar electrodes were successfully coated by the polyimide layer except that the top surface area was not coated. However, some sidewall areas near the top surface were not covered perfectly. Figure 18 shows the impedance characteristics of isolated and non-isolated pillar electrodes depending on the frequency. The impedance of the non-isolated pillar electrode is 24.6 kΩ, whereas the impedance of the isolated pillar electrode is 116 kΩ at 1 kHz, respectively. The impedance of the isolated pillar electrode is similar to the impedance of the planar electrode of 125 kΩ at 1 kHz (as shown in figure 14). It indicates that the sidewall of the pillar electrode was isolated well by the polyimide layer; therefore, the top surface area of the pillar electrode functioned solely as the stimulus electrode. Ideally, the impedances of the isolated pillar electrode and the planar electrode should be the same. However, the impedance of the isolated pillar electrode is a little small, because some sidewall area near the top surface was not covered (as shown in figure 17). The increased surface

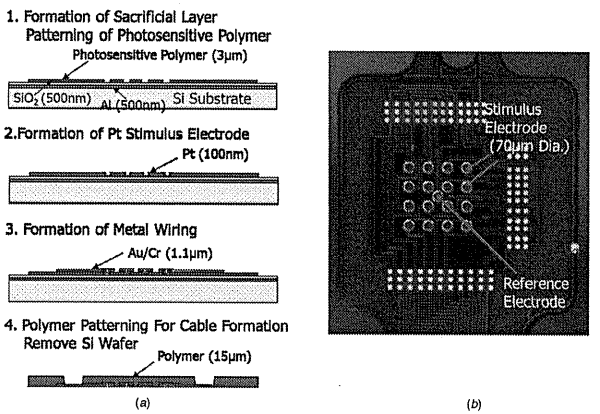

Figure 13. (*a*) The fabrication process and (*b*) the photograph of the flexible cable with the Pt planar electrode array.

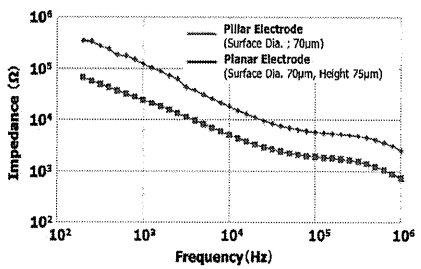

Figure 14. Impedance spectra of the planar electrode and the pillar electrode with 70 μm diameter size depending on frequencies.

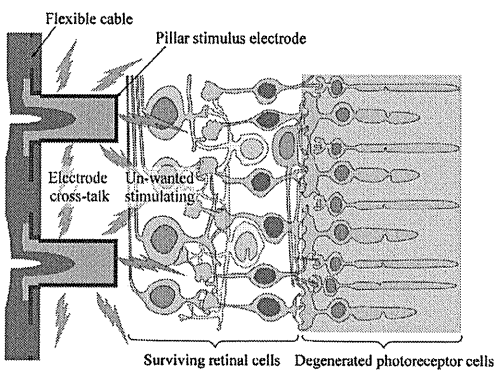

Figure 15. Concept of electrode cross-talk of a pillar stimulus electrode.

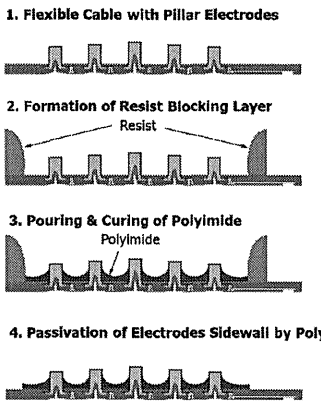

Figure 16. The sidewall isolation process flow of a pillar electrode.

area (4145 μm^2) induces decreased impedance than the planar electrode (3846 μm^2). However, this result shows a potential issue of differing impedances of the isolated pillar electrodes in the MEA. It is necessary to improve the sidewall passivation process.

To characterize the spherical conformity of the pillar electrode, the contacting behaviors of the pillar-shaped stimulus MEA and the planar stimulus MEA were evaluated. The fabricated MEA pricked an agar gel, which was cured into a spherical shape. A 2.5% agar has Young's modulus of 22 kPa [34], which is similar to Young's modulus of the retina (20 kPa) [35]. An agar gel (2.5%) was composed and then cured into an eyeball shape with a spherical mold [33]. The planar and the pillar stimulus MEAs were attached on the inside of the spherical-shaped agar, respectively. After detaching the curved MEAs, the agar surfaces were measured using an optical microscope as shown in figure 19. In the case of the planar MEA, any shape of the electrodes was not observed

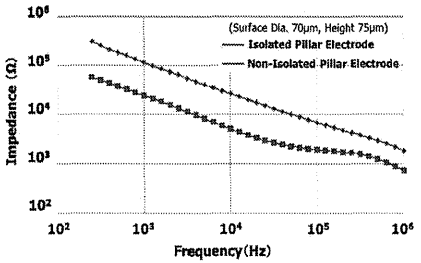

Figure 18. Impedance spectra of isolated and non-isolated pillar electrodes depending on frequencies.

from the agar surface as shown in 19(*a*). In the case of the pillar MEA, meanwhile, the extruded electrode array pattern was observed from the agar surface as shown in 19(*b*). However, the extruded array pattern is not clear and non-uniform. We assume that the pillar MEA was contacted manually to the agar surface, and therefore, it was not uniformly in contact with the agar surface. Even the electrode impression results are not clear sufficiently, we understand the difference of the conformity characteristics between the planar MEA and the pillar MEA. This shows the advantage achieved by highly efficient stimulation to the retina cells in the spherical eyeball.

In this study, we implemented the pillar-shaped stimulus MEA with varying heights to improve the stimulation efficiency to the retina cells and, consequently, induce highly qualitative resolution of the retinal prosthesis. However, this epiretinal approach, in which the device is implanted into the vitreous cavity and attached to the inner retinal surface, has relevant issues such as possible difficulties in chronic attachment of the 3D stacked retinal prosthesis to the retina. It requires optimization of the epiretinal design and improvement of surgical techniques for realizing the fully implantable epiretinal prosthesis.

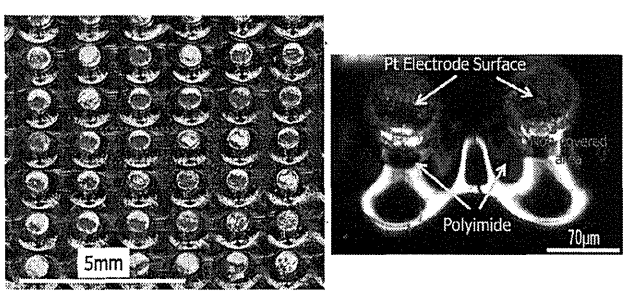

Figure 17. Photographs of the pillar electrode array partially coated by a biocompatible polyimide layer.

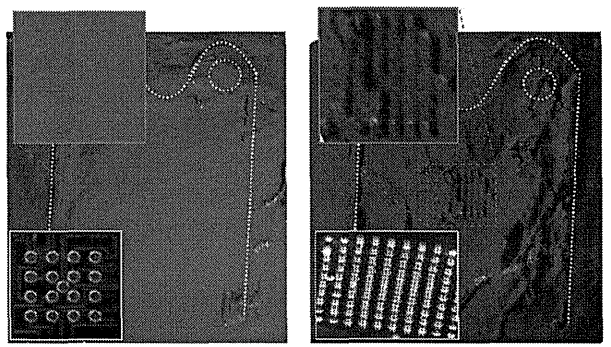

Figure 19. The agar gel surfaces after attaching (*a*) the planar MEA and (*b*) the pillar MEA, respectively.

4. Conclusion

The pillar-shaped stimulus MEA with varying heights was fabricated for enhancing the spherical conformity of the fully implantable epiretinal prosthesis. The fabricated MEA is composed of 100 pillar electrodes with heights ranging from 60 to 80 μm. The Pt-coated Cu pillar electrode with a surface diameter of 70 μm and a height of 75 μm and the Pt planar electrode with a surface diameter of 70 μm have 24.6 and 125 kΩ impedances, respectively, at 1 kHz *in vitro* experiment. The pillar electrode shows lower impedance than the planar electrode because of a large electrode surface area. However, to avoid cross-talking between pillar electrodes, we developed a sidewall passivation process of the pillar electrode by using the surface tension of polyimide. The impedance of the isolated pillar electrode 116 kΩ at 1 kHz is similar to the impedance of the planar electrode, because they have similar electrode surface areas. The pillar-shaped MEA shows a better spherical conformity.

Acknowledgments

This work was supported by Japan Society for the Promotion of Science (JSPS), grant-in-aid for Scientific Research 'Grant-in-Aid for Scientific Research (B)', no 21226009. This work was performed in the Micro/Nano-Machining Research Center (MNC), Tohoku University.

References

[1] Santos A, Humayun M S Jr, Greenburg R J, de Juan E, Marsh M J, Klock I B and Milam A H 1997 *Arch. Ophthalmol.* **115** 511–5
[2] Medeiros N E and Curcio C A 2001 *Invest. Ophthalmol. Vis. Sci.* **42** 795–803
[3] Humayun M S, Dagnelie G Jr, de Juan E, Greenberg R J, Propst R H and Phillips H 1996 *Arch. Ophthalmol.* **114** 40–6
[4] Chow A Y and Chow V Y 1997 *Neurosci. Lett.* **225** 13–6
[5] Eckmiller R 1997 *Ophthalmic Res.* **29** 281–9
[6] Zrenner E *et al* 1997 *Ophthalmic Res.* **29** 269–80
[7] Zrenner E 2002 *Science* **295** 1022–5
[8] Humayun M S, Propst R, de Juan E, McCormick K Jr and Hickingbotham D 1994 *Arch. Ophthalmol.* **112** 110–6
[9] Wyatt J and Rizzo 1996 *IEEE Spectr.* **33** 47–53
[10] Chow A Y and Peachey N S 1998 *Ophthalmic Res.* **30** 195–6
[11] Liu W, Vichienchom K, Clements M, DeMarco S C, Hughes C, McGucken E, Humayun M S, de Juan E, Weiland J D and Greenberg R 2000 *IEEE J. Solid-State Circuits* **35** 1487–97
[12] Margalit E *et al* 2003 *J. Neurosci. Methods* **123** 129–37
[13] Humayun M S, Juan E, Weiland J E, Dagnelie G, Katona S, Greenberg R and Suzuki S 1999 *Vis. Res.* **39** 2569–76
[14] Ohta J, Yoshida N, Kagawa K and Nunoshita M 2002 *Japan. J. Appl. Phys.* **41** 2322–5
[15] Scribner D *et al* 2007 *IEEE Trans. Biomed. Circuits Syst.* **1** 73–83
[16] Schanze T, Hesse L, Lau C, Greve N, Haberer W, Kammer S, Doerge T, Rentzos A and Stieglitz T 2007 *IEEE Trans. Biomed. Circuits Syst.* **54** 983–92
[17] Zrenner E 2002 *Ophthalmologica* **216** 8–20
[18] Kurino H, Lee K W, Nakamura T, Sakuma K, Park K T, Miyakawa N, Shimazutsu H, Kim K Y, Inamura K and Koyanagi M 1999 *Int. Electron Devices Meeting Technical Digest* pp 879–82
[19] Chow A Y, Chow V Y, Packo K H, Pollack J S, Peyman G A and Schuchard R 2004 *Arch. Ophthalmol.* **122** 460–9
[20] Chow A Y, Bittner A K and Pardue M T 2010 *Trans. Am. Ophthalmol. Soc.* **108** 120–54
[21] Zrenner E *et al* 2010 *Proc. R. Soc.* B **278** 1489–97
[22] Koyanagi M, Nakagawa Y, Lee K W, Nakamura T, Yamada Y, Inamura K, Park K T and Kurino H 2001 *Int. Solid-State Circuit Conf. Digest of Technical Papers* pp 270–1
[23] Deguchi J, Watanabe T, Motonami K, Sugimura T, Tomita H, Shim J C, Kurino H, Tamai M and Koyanagi M 2004 *Int. Conf. on Solid State Devices and Materials (Extended Abstracts)* pp 350–1

[24] Deguchi J, Watanabe T, Nakamura T, Nakagawa Y, Fukushima T, Shim J C, Kurino H, Abe T, Tamai M and Koyanagi M 2004 *Japan. J. Appl. Phys.* **43** 1685–9
[25] Motonami K, Watanabe T, Deguchi J, Fukushima T, Tomita H, Sugano E, Sato M, Kurino H, Tamai M and Koyanagi M 2006 *Japan. J. Appl. Phys.* **45** 3784–8
[26] Watanabe T, Kobayashi R, Komiya K, Fukushima T, Tomit H, Sugano E, Kurino H, Tanaka T, Tamai M and Koyanagi M 2007 *Japan. J. Appl. Phys.* **46** 2785–91
[27] Tanaka T, Sato K, Komiya K, Kobayashi T, Watanabe T, Fukushima T, Tomita H, Kurino H, Tamai M and Koyanagi M 2007 *Int. Electron. Devices Meeting Tech. Digest* pp 1016–9
[28] Abuja A K, Behrend M R, Kuroda M, Humayun M S and Weiland J D 2008 *IEEE Trans. Biomed. Eng.* **55** 1744–53
[29] Margalit E *et al* 2002 Surv. Ophthalmol. **47** 335–6
[30] Humayun M S 2001 *Trans. Am. Ophthalmol. Soc.* **99** 271–300
[31] Hungar K, Gortz M, Slavcheva E, Spainer G, Weidig C and Mokwa W 2005 *Sensors Actuators* A 172–8
[32] Wang R, Huang X, Liu G, Wang W, Dong F and Li Z 2010 *J. Microelectromech. Syst.* **19** 367–74
[33] Koo K, Lee S, Bae S, Seo J, Chung H and Cho D 2011 *J. Microelectromech. Syst.* **20** 251–9
[34] Stolz M, Raiteri R, Daniels A U, VanLandingham M R, Baschong W and Aebi U 2004 *Biophys. J.* **86** 3269–83
[35] Jones I L, Warner M and Stevens J D 1992 *Eye* **6** 556–9

Contents lists available at ScienceDirect

Sensors and Actuators B: Chemical

journal homepage: www.elsevier.com/locate/snb

Development and characterisation of a compact light-addressable potentiometric sensor (LAPS) based on the digital light processing (DLP) technology for flexible chemical imaging

Torsten Wagner[a,*], Carl Frederik Werner[b,c], Ko-ichiro Miyamoto[a], Michael J. Schöning[b,c], Tatsuo Yoshinobu[a,d]

[a] Department of Electronic Engineering, Tohoku University, Japan
[b] Institute of Nano- and Biotechnologies, Aachen University of Applied Sciences, Germany
[c] Institute of Bio- and Nanosystems-2, Research Centre Jülich, Germany
[d] Department of Biomedical Engineering, Tohoku University, Japan

ARTICLE INFO

Article history:
Available online 24 December 2010

Keywords:
Digital light processing (DLP)
Light-addressable potentiometric sensor (LAPS)
Chemical imaging
Chemical sensor

ABSTRACT

Chemical imaging systems allow the visualisation of the distribution of chemical species on the sensor surface. This work represents a new flexible approach to read out light-addressable potentiometric sensors (LAPS) with the help of a digital light processing (DLP) set-up. The DLP, known well for video projectors, consists of a mirror-array MEMS device, which allows fast and flexible generation of light patterns. With the help of these light patterns, the sensor surface of the LAPS device can be addressed. The DLP approach has several advantages compared to conventional LAPS set-ups, e.g., the spot size and the shape of the light pointer can be changed easily and no mechanical movement is necessary, which reduces the size of the set-up and increases the stability and speed of the measurement. In addition, the modulation frequency and intensity of the light beam are important parameters of the LAPS set-up. Within this work, the authors will discuss two different ways of light modulation by the DLP set-up, investigate the influence of different modulation frequencies and different light intensities as well as demonstrate the scanning capabilities of the new set-up by pH mapping on the sensor surface.

1. Introduction

The light-addressable potentiometric sensor (LAPS) consists of a photosensitive semiconductor structure. The semiconductor structure shares a liquid/solid interface with the analyte solution (see Fig. 1a). By applying a dc bias voltage across the sensor set-up, a photocurrent will be generated. This photocurrent depends mainly on the light stimulus, the local electrochemical parameters at the solid/liquid interface (e.g., the concentration of a certain ion) and the applied bias voltage. The intensity of the light source needs to be modulated to generate a continuous external ac photocurrent. Keeping both the amplitude of the alternating light stimulus and the bias voltage constant, the analyte concentration can be determined by measuring the amplitude [1] or the phase [2] of the resulting photocurrent. The photocurrent consists of the same frequency as the light stimulus. Thus, for both methods, the signal quality can be enhanced by filtering unwanted frequency components due to external disturbances, e.g., with a FFT (fast Fourier transformation) filter or a PLL (phase-lock loop) circuit to determine the photocurrent amplitude peak only at the modulation frequency of the stimulus. To address different regions on the sensor surface, the position of the light pointer can be changed accordingly. More information about the LAPS principle can be found elsewhere [3,4].

Chemical imaging systems scan the complete surface of a LAPS structure in a raster-form manner. The resulting photocurrent at each measurement spot will be mapped into a colour representation and images of the electrochemical properties at the sensor surface can be generated. Those images were successfully created, e.g., to depict the acidification due to the metabolic activity of cell cultures [5], to visualise electrochemical processes [6,7] and enzymatic reactions [8], or to observe fluidic processes in microfluidic devices [9].

Conventional chemical imaging systems require a mechanical XY-stage and a single focused laser beam to address the measurement spots one-by-one (see Fig. 1a). This first generation of scanning LAPS devices had the drawback to be rather bulky in size and rather slow due to the mechanical movement of the XY-stage. Furthermore, the shape and size of the light pointer were fixed by the light source's optique and hence, unchangeable during the measurement.

Recent approaches utilise VCSEL (vertical cavity surface emission laser) diodes [10] or OLED (organic light emitting diodes) displays [11] to miniaturise and increase the speed of the set-up. However, both methods have the drawback of being rather limited in the amount of individually addressable light sources. As an alternative, the authors introduced a new approach utilising a DLP[1]-based set-up [12] to generate chemical images with free definition of the light pointer by means of the size and shape (see Fig. 1b). This enables a careful adjustment of the trade-off between the measurement speed and the resolution of the generated images. A set-up to generate conductive electrodes on a semiconductor structure by means of a constant light beam based on a DMD[2] was suggested by Suzurikawa et al. [13]. Ipatov et al. demonstrated preliminary results of a DMD-based LAPS set-up independently from the authors, combining a modulated laser source and a DLP-based video projector for pattern generation [14]. More information about chemical imaging based on LAPS devices can be found elsewhere [4,15–17].

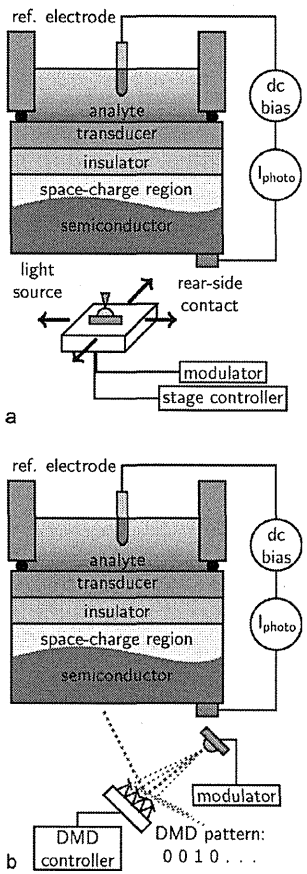

Fig. 1. Schematics of different scanning LAPS set-ups. (a) Conventional set-up with a single light source and an XY-stage to address different regions on the sensor chip. (b) New set-up with a more flexible light source based on a DLP. The position and size of the measurement spot can be modified as required.

2. Experimental

The generation of light patterns to form sensor spots by DLP-based projection has the advantage to provide a much higher contrast ratio compared to other shape-forming methods like, e.g., LCD-based projectors, which is essential for LAPS set-ups. Only for a high contrast ratio, the majority of the generated photocurrent can be assigned to the intended measurement spot. To generate an externally detectable photocurrent, the light intensity needs to be modulated. Thus, beside the shape of the light spots, the modulation frequency is an important key parameter of the LAPS set-up [18–20]. In principle, the DLP technology offers two different methods to modulate the generated light patterns. The DMD chip consists of an array of micro-mirror devices which can be flipped to only one of two distinct tilt positions. In the first method, the mirrors of the DMD chip (see Fig. 2a) are set to a static mirror pattern and the internal light source will be modulated. The generated light will be reflected depending on the fixed pattern of the DMD mirrors. Thus, the light will be either reflected into an optical absorber unit, or guided towards an opening window, from which the modulated light passes an optical set-up and finally arrives with the desired shape at the sensor rear side. In the second method, a light source with a constant intensity will be reflected by a fast switching DMD mirror pattern. Thus, the light beam will be alternately guided to the absorber and to the output window (see Fig. 2b).

Whereas the first method is relatively easy to implement, it has the drawback that any misguided light and any unintentional reflections, e.g., at the DMD-chip substrate and DMD enclosure might be finally reflected towards the output window. Such reflections would contribute significantly to the generated photocurrent and since they have the same modulation frequency as the desired measurement spot, they can not be removed from the resulting photocurrent by means of filtering. The second method requires a much higher access to the DMD array to refresh the mirror pattern at high speeds. However, only the alternating mirror pattern will be contributing to the modulation of the light beam, unintended reflections will remain unmodulated and thus, their contribution to the photocurrent signal can be filtered. This promises a much better signal-to-noise ratio. In this work, the authors applied the second method and generated the light modulation in addition to spot size and the spot shape by the DMD mirror pattern.

A DLP system (Pico V2 development kit, Texas Instruments) is installed underneath the LAPS structure. A Ag/AgCl reference electrode and a rear-side gold contact are utilised to apply the bias voltage and to record the generated photocurrent. The measurement spot is defined in size, shape and position by addressing certain mirrors on the DMD chip to form the desired image pattern.

* Corresponding author at: 6-6-05 Aza-Aoba, Aramaki, Aoba-ku, Sendai, Miyagi 980-8579, Japan.
E-mail addresses: wagner@ecei.tohoku.ac.jp, torsten.wagner@fh-aachen.de (T. Wagner).
URL: http://www.bme.ecei.tohoku.ac.jp (T. Wagner).

0925-4005/$ – see front matter © 2010 Elsevier B.V. All rights reserved.
doi:10.1016/j.snb.2010.12.003

[1] Digital light processing, a trademark of Texas Instruments to describe the entire electronic platform to process video data and to control the included DMD chip.
[2] Digital mirror device.

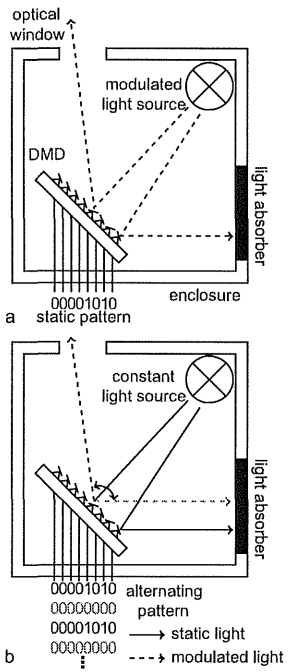

Fig. 2. Two different methods to modulate the light intensity by means of a DLP set-up. (a) Modulated light source reflected by a static mirror pattern on the DMD to form the desired pattern shapes. (b) Constant light source reflected by fast switching mirrors to generate a modulated light pattern.

The image pattern is generated independent of the measurement PC on an ARM-based processor board (beagle-board) executing a home-made program on a GNU/Linux-based operating system. This guarantees accurate timing of the patterns independent of the PC workload. The PC is capable of sending commands to the DLP controller over a serial interface. No mechanical movement (except for the tilt of the micro-mirrors) is necessary. The present set-up can address 480 × 320 pixels, which results in a maximum resolution of 153.600 measurement spots. The spot size and shape can be freely defined according to the measurement task, without any modification of mechanical parts of the set-up itself.

The generated photocurrent is first passed through a transimpedance amplifier and then sampled by an A/D converter (DAQ-card from National Instruments). A home-made LabVIEW-based software assist to generate the desired bias voltage, to record the resulting photocurrent, to determine the frequency components at the modulation frequency of the light beam and to send commands to the DLP-controller board to change the parameters of the measurement spot. For the chemical imaging, the software includes the translation of the detected photocurrent into a colour-map representation.

Table 1
Possible modulation frequencies generated by the 24 bit patterns of the Pico V2 DLP kit.

Bit pattern	Theo. frequency (Hz)
10101010.10101010.10101010	720
11001100.11001100.11001100	360
11100011.10001110.00111000	240
11110000.11110000.11110000	180
11111100.00001111.11000000	120
11111111.11110000.00000000	60

The Pico V2 development kit grants access to some of the internal DMD-control processes and registers via an I2C (inter-integrated circuit)-bus interface. This enables the controller program on the beagle-board to switch the system between a standard projector mode with a fixed image refresh rate of 60 Hz and 24-bit colour (red, green and blue with 8-bit resolution) and a monochromatic light mode (structured light mode) at an image rate of 1440 Hz. Typically, video projectors apply different image filters within the DLP logic to generate a pleasant video experience. In the case of scanning LAPS, it will be necessary to bypass all these internal filters in the internal DLP logic inside the projector to guarantee an unmodified one-by-one mapping of the input image and the final micro-mirror array pattern. Furthermore, the DLP-controller board can access internal registers to adjust the currents of the LED-based light source of the Pico-projector.

The above described structured light mode has the possibility to use different modulation frequencies. The frequencies are generated by converting the colour of a single pixel into a 24-bit long timing sequence for a monochromatic image, which will be displayed by the projector at a frequency of 1440 Hz (60 Hz × 24). Thus, sending alternating '1' and '0' patterned results in a modulation frequency of 720 Hz. To create a continuous modulation, the bit pattern (duty ratio = 0.5) has to fit entirely into the 24-bit word. Table 1 shows all possible bit patterns with the corresponding modulation frequencies. It has to be noted, that the real frequencies could be slightly off compared to the theoretical values due to tolerances of the 60 Hz video input sync signal.

In addition to the focusing system of the projector, a lens was installed between the projector and the LAPS structure to generate a measurement area of 20.8 mm × 15.6 mm. The active LAPS surface was defined by the opening window of the rear-side contact to be 28 mm × 28 mm. For the *I*/*V* (photocurrent *vs.* voltage) curve measurements, the bias voltage was swept between −2.5 V and 0 V. Keeping the bias potential constant at −1 V, chemical images were obtained for different measurement spot sizes of 10 × 10, 5 × 5, 3 × 3 pixels with equivalent step width, and a measurement with 3 × 3 pixels with 1 pixel step width, respectively. Table 2 summarises the parameters for the different chemical images. All scans were obtained for a pH 7 solution utilising the red LED of the projector at a modulation frequency of 713 Hz.

The frequency components of the resulting photocurrents were analysed for each measurement spot and stored together with the spot coordinates. Finally, the photocurrent was normalised and a colour representation was generated. The surface of the LAPS structure (same structure as for the *I*/*V* measurements) was modified by a polymer resist to locally modify the sensor impedance as a test pattern.

Table 2
Measurement parameters for the scanning LAPS images depicted in Fig. 6

Measurement spot size		Step width (μm)	Array dimension spots	Number of spots
Pixels	μm²			
10 × 10	434 × 434	434	48 × 32	1,536
5 × 5	217 × 217	217	96 × 64	6,144
3 × 3	130 × 130	130	160 × 106	16,960
3 × 3	130 × 130	43	478 × 319	152,482

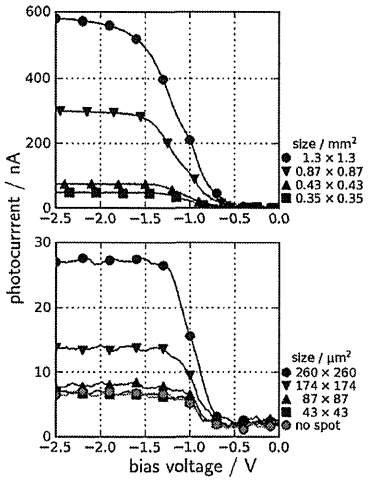

Fig. 3. Photocurrent vs. bias voltage (*I*/*V*) plots for different measurement spot sizes defined by the DLP set-up for a pH-sensitive LAPS structure at pH 7.

3. Results and discussion

Fig. 3a and b depict typical *I*/*V* curves of a pH-sensitive LAPS structure (n-Si/SiO_2/Si_3N_4) for a pH 7 buffer solution (Titrisol) measured with different square-shaped measurement spots between 1 × 1 pixel and 30 × 30 pixels in size. Thus, the measurement spot area varied between 1.88 × 10^{-3} mm^2 and 1.69 mm^2. The figures show a clear *I*/*V* curve behaviour for spot sizes down to 4 × 4 pixels, corresponding to 174 × 174 μm^2. It was noticed that the total amount of photocurrent was smaller compared to set-ups based on focused laser sources [10]. Although the theoretical optical resolution of the present system could be calculated to be as small as 43 μm^2 for a single pixel, at the present system, measurement spots smaller than 3 × 3 pixels did not provide sufficient light to distinguish between light spots and background illumination. However, the present measurement spot size limit of about 130 × 130 μm^2 is already in the range of the spatial resolution of conventional LAPS sensors [21–24]. The use of resolution-optimised LAPS structures together with an infrared light source [21] and a specially designed DMD system with a tailored optique might allow the use of even smaller measurement spots.

As discussed in Section 2, the DMD technology provides a high contrast ratio between active and dark regions. The contrast ratio for the pico V2 kit is according to the data sheet 1:1000. Fig. 4a depicts *I*/*V* curves for different LED brightnesses (adjusted by the LED current for a spot size of 0.87 mm × 0.87 mm (20 × 20 pixels), modulated at 713 Hz. Fig. 4b illustrates the same measurements with all pixels set to "off". Since the light source is still turned on, a certain background illumination occurs.

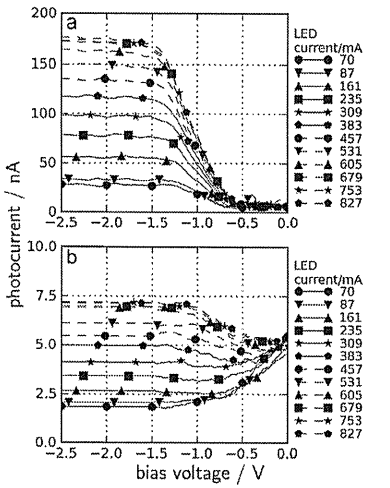

Fig. 4. (a) *I*/*V* curves at pH 7 for a spot size of 0.87 mm × 0.87 mm (20 × 20 pixels) for different light intensities of the DMD light source. (b) *I*/*V* curve measurements at different light intensities with all pixels set to "off" to determine the effect of the background illumination.

The photocurrent can be adjusted and possibly further increased by increasing the light intensity of the DLP light source, as shown in Fig. 4a. For higher light intensities an optimised optical set-up would be required in addition to reduction of background light effects which occur as shown in Fig. 4b. An improvement of the light intensity and reducing of light scattering would result in a

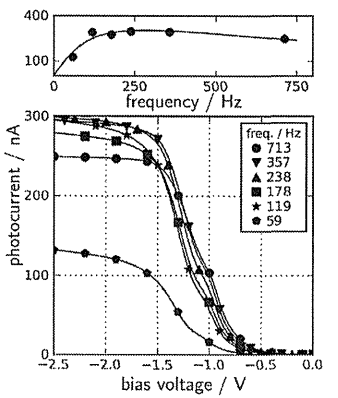

Fig. 5. *I*/*V* curve characteristic (bottom) of the new DLP-based set-up for different modulation frequencies. The upper plot indicates the bandpass characteristics of the LAPS structure.

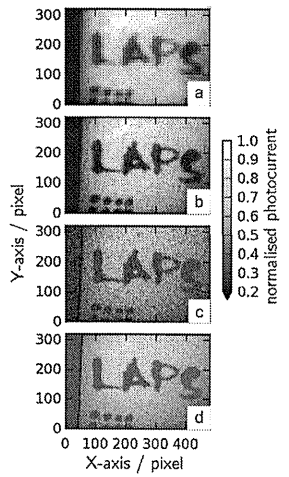

Fig. 6. Chemical imaging at pH 7 for different measurement spot sizes and step widths according to Table 2. (a) 10 × 10 pixels, (b) 5 × 5 pixels, (c) 3 × 3 pixels and (d) 3 × 3 pixels with a step width of 1 pixel; total image size is 20.8 mm × 15.6 mm.

better signal-to-noise ratio, which would allow even smaller measurement spot sizes.

Fig. 5 shows the resulting *I/V* curves at pH 7 for modulation frequencies between 59 Hz and 713 Hz generated by the DMD. The spot size was set to be 20 × 20 pixels equivalent to 0.87 mm × 0.87 mm. The DLP kit in its present form does only allow to set-up modulation frequencies of certain values as depicted in Table 2 and Fig. 5. Due to the bandpass characteristic of the LAPS structure, the choice of the correct modulation frequency is essential to obtain the best signal-to-noise ratio [25–27]. Thus, a more direct control of the DLP system in terms of light source intensity as well as modulation frequency would be beneficial.

The scanning images in Fig. 6 demonstrate the possibility to generate images of chemical reactions that occur at the sensor surface. Starting from Fig. 6a each successive image depicts a higher grade of detail due to the definition of a higher density of measurement spots. The scanning parameters for the individual images can be found in Table 2. The length of the "LAPS" lettering was about 15.8 mm. A single scanning line of this lettering consist of 36 up to 364 measurement spots, respectively. The dots in the lower left corner have an average diameter of 1.3 mm and their area is scanned by a maximum of about 600 measurement spots each for the highest resolution scan.

4. Summary and conclusions

These first characteristics prove the good performance of the new DLP-based LAPS set-up for chemical imaging. In addition to the achieved reduction of the set-up size and the increase of measurement speed, the flexible generation of the light patterns to define different shapes and sizes of measurement spots are advantageous compared to former set-ups. The home-made software will take advantage of the flexible light set-up by enabling the operator to overlay different chemical images. The authors investigate a method, where a first quick scan with a low resolution can be performed within seconds for the complete sensor surface. After that, smaller regions of interest could be scanned with a higher resolution, which offers the possibility to obtain more detailed information, just where needed. For example, a scan of the complete scanning region of 20.8 mm × 15.6 mm with a measurement spot size of 2.6 mm × 2.6 mm takes only two seconds. A scan of a smaller subset of the scanning area like 5 mm × 5 mm with a measurement spot size of 0.87 mm × 0.87 mm would take approximately 5 s. A final "zoom" down to an area of interest of the size of 1 mm × 1 mm, with a measurement spot size of only 130 μm × 130 μm would take about one minute. Thus, this "zoom-in" method is promising to combine the benefits of a fast chemical imaging and high resolution scans. Furthermore, ongoing research is dealing how to utilise generated chemical images for a fast classification of multicomponent analytes. One possibility would be the combination of an array of measurement spots with virtually, arbitrary different sensor characteristics on a single LAPS structure and the application of well-studied image recognition algorithms. This method could compare images of known analyte composition to an unknown analyte composition and determine similarities and differences for a final classification.

Acknowledgement

The authors gratefully thank the Japan Society for the Promotion of Science for the financial support.

References

[1] D. Hafeman, J. Parce, H. McConnell, Light-addressable potentiometric sensor for biochemical systems, Science 240 (4856) (1988) 1182–1185.
[2] K. Miyamoto, T. Wagner, T. Yoshinobu, S. Kanoh, M.J. Schöning, Phase-mode LAPS and its application to chemical imaging, Sensors and Actuators B: Chemical, in press, doi:10.1109/SENSOR.2009.5285704.
[3] J.C. Owicki, L.J. Bousse, D.G. Hafeman, G.L. Kirk, J.D. Olson, H.G. Wada, J.W. Parce, The light-addressable potentiometric sensor: principles and biological applications, Annual Review of Biophysics and Biomolecular Structure 23 (1994) 87–113.
[4] T. Wagner, M.J. Schöning, Light-addressable potentiometric sensors (LAPS): recent trends and applications, in: S. Alegret, A. Merkoci, (Eds.), Electrochemical Sensor Analysis, vol. 49, Elsevier, 2007, pp. 87–128 (Chapter 5).
[5] M. Nakao, S. Inoue, R. Oishi, T. Yoshinobu, H. Iwasaki, Observation of microorganism colonies using a scanning-laser-beam pH-sensing microscope, Journal of Fermentation and Bioengineering 79 (2) (1995) 163–166.
[6] T. Yoshinobu, H. Iwasaki, M. Nakao, S. Nomura, T. Nakanishi, S. Takamatsu, K. Tomita, Application of chemical imaging sensor to electro generated pH distribution, Japanese Journal of Applied Physics Part 2—Letters and Express Letters 37 (3B) (1998) L353–L355.
[7] T. Yoshinobu, T. Harada, H. Iwasaki, Application of the pH-imaging sensor to determining the diffusion coefficients of ions in electrolytic solutions, Japanese Journal of Applied Physics Part 2—Letters 39 (4A) (2000) L318–L320.
[8] S. Inoue, M. Nakao, T. Yoshinobu, H. Iwasaki, Chemical-imaging sensor using enzyme, Sensors and Actuators B: Chemical 32 (1) (1996) 23–26.
[9] T. Yoshinobu, H. Iwasaki, Y. Ui, K. Furuichi, Y. Ermolenko, Y. Mourzina, T. Wagner, N. Näther, M.J. Schöning, The light-addressable potentiometric sensor for multi-ion sensing and imaging, Methods 37 (1) (2005) 94–102.
[10] T. Wagner, C. Werner, K. Miyamoto, M. Schöning, T. Yoshinobu, A high-density multi-point LAPS set-up using a VCSEL array and FPGA control, Procedia Chemistry 1 (1) (2009) 1483–1486.
[11] K. Miyamoto, K. Kaneko, A. Matsuo, T. Wagner, S. Kanoh, M. Schöning, T. Yoshinobu, Miniaturized chemical imaging sensor system using a OLED display panel, Procedia Engineering 5 (1) (2010) 516–519.
[12] T. Wagner, K. Miyamoto, C. Werner, M. Schöning, T. Yoshinobu, Utilising digital micro mirror device (DMD) as scanning light source for light-addressable potentiometric sensors (LAPS), in: 13th International Meeting on Chemical Sensors, 2010, pp. 0–4.
[13] J. Suzurikawa, M. Nakao, R. Kanzaki, H. Takahashi, Microscale pH gradient generation by electrolysis on a light-addressable planar electrode, Sensors and Actuators B: Chemical 149 (1) (2010) 205–211.
[14] A. Ipatov, K. Zinoviev, N. Abramova, A. Bratov, Light addressable potentiometric sensor array: a new approach for light beam positioning, Procedia Engineering 5 (1) (2010) 625–628.
[15] T. Yoshinobu, H. Ecken, A.B.Md. Ismail, H. Iwasaki, H. Lüth, M.J. Schöning, Chemical imaging sensor and its application to biological systems, Electrochimica Acta 47 (1–2) (2001) 259–263.

[16] D. Filippini, J. Gunnarsson, I. Lundström, Chemical image generation with a grid-gate device, Journal of Applied Physics 96 (12) (2004) 7583–7590.
[17] D. Filippini, I. Lundström, H. Uchida, Gap-gate field effect gas sensing device for chemical image generation, Applied Physical Letters 84 (15) (2004) 2946–2948.
[18] M. Sartore, M. Adami, C. Nicolini, L. Bousse, S. Mostarshed, D. Hafeman, Minority carrier diffusion length effects on light-addressable potentiometric sensor (LAPS) devices, Sensors and Actuators A: Physical 32 (1–3) (1992) 431–436.
[19] L. Bousse, S. Mostarshed, D. Hafeman, M. Sartore, M. Adami, C. Nicolini, Investigation of carrier transport through silicon wafers by photocurrent measurements, Journal of Applied Physics 75 (8) (1994) 4000–4008.
[20] W. Hu, H. Cai, J. Fu, P. Wang, G. Yang, Line-scanning LAPS array for measurement of heavy metal ions with micro-lens array based on MEMS, Sensors and Actuators B: Chemical 129 (1) (2008) 397–403.
[21] M. Nakao, S. Inoue, T. Yoshinobu, H. Iwasaki, High-resolution pH imaging sensor for microscopic observation of microorganisms, Sensors and Actuators B: Chemical 34 (1–3) (1996) 234–239.
[22] W.J. Parak, U.G. Hofmann, H.E. Gaub, J.C. Owicki, Lateral resolution of light-addressable potentiometric sensors: An experimental and theoretical investigation, Sensors and Actuators A: Physical 63 (1) (1997) 47–57.
[23] W. Moritz, I. Gerhardt, D. Roden, M. Xu, S. Krause, Photocurrent measurements for laterally resolved interface characterization, Fresenius' Journal of Analytical Chemistry 367 (4) (2000) 329–333.
[24] L. Chen, Y. Zhou, S. Jiang, J. Kunze, P. Schmuki, S. Krause, High resolution LAPS and SPIM, Electrochemistry Communications 12 (6) (2010) 758–760.
[25] Q. Zhang, P. Wang, W.J. Parak, M. George, G. Zhang, A novel design of multi-light LAPS based on digital compensation of frequency domain, Sensors and Actuators B: Chemical 73 (2–3) (2001) 152–156.
[26] T. Wagner, R. Molina, T. Yoshinobu, J.P. Kloock, M. Biselli, M. Canzoneri, T. Schnitzler, M.J. Schöning, Handheld multi-channel LAPS device as a transducer platform for possible biological and chemical multi-sensor applications, Electrochimica Acta 53 (2) (2007) 305–311.
[27] K. Miyamoto, Y. Kuwabara, S. Kanoh, T. Yoshinobu, T. Wagner, M.J. Schöning, Chemical image scanner based on FDM-LAPS, Sensors and Actuators B: Chemical 137 (2) (2009) 533–538.

Biographies

Torsten Wagner was born in Mönchengladbach, Germany, in 1978. He received his diploma in 2003 in electrical engineering from the University of Applied Sciences Aachen, his master of science in 2003 in model simulation and control from the Coventry University in UK, and his doctoral degree (PhD) in 2008 from the Philipps University Marburg in cooperation with the University of Applied Sciences Aachen. His research subjects concern chemical sensors, especially the light-addressable potentiometric sensor and sensor-signal processing. He received a scholarship (2008–2010) from the Japanese Society for the Promotion of Sciences (JSPS) to work at the Tohoku University in Japan, at which he became 2010 an assistant professor.

Frederik Werner was born in Göttingen, Germany, in 1982. He received his diploma in 2008 in micro system technology from the University of Applied Sciences Kaiserslautern. He started his PhD thesis in 2008 at the Institute of Nano- and Biotechnologies (Aachen University of Applied Sciences). His research subjects concern chemical and biological sensors, especially the light-addressable potentiometric sensor together with micro-organisms and sensor-signal processing.

Ko-ichiro Miyamoto was born in Yamaguchi, Japan, in 1979. He received BE, ME, and PhD degrees from Tohoku University in 2002, 2004 and 2006, respectively. His PhD degree is for his study on the bio-molecular sensing using infrared absorption spectroscopy. Since 2006, he is an assistant professor in the Department of Electronic Engineering, Tohoku University. His research subject is on the application of silicon-based chemical sensors for bio-molecular sensing.

Michael J. Schöning received his diploma degree in electrical engineering (1989) and his PhD in the field of semiconductor-based microsensors for the detection of ions in liquids (1993), both from the Karlsruhe University of Technology. In 1989, he jointed the Institute of Radiochemistry at the Research Centre Karlsruhe. Since 1993, he has been with the Institute of Thin Films and Interfaces (now, Institute of Bio and Nanosystems) at the Research Centre Jülich, and since 1999 he was appointed as full Professor at Aachen University of Applied Sciences, Campus Jülich. Since 2006, he serves as a director of the Institute of Nano- and Biotechnologies (INB) at the Aachen University of Applied Sciences. His main research subjects concern silicon-based chemical and biological sensors, thin-film technologies, solid-state physics, microsystem and nano(bio-)technology.

Tatsuo Yoshinobu was born in Kyoto, Japan, in 1964. He received BE, ME, and PhD degrees in electrical engineering from Kyoto University in 1987, 1989, and 1992, respectively, for his study on gas source molecular beam epitaxy of silicon carbide. In 1992, he joined the Institute of Scientific and Industrial Research, Osaka University, where he started the development of silicon-based chemical sensors. From 1999 to 2000, he was a guest scientist at the Research Centre Jülich, Germany. Since 2005, he is a professor for electronic engineering at Tohoku University, Sendai, Japan. Since 2008, he is also a professor at the Graduate School of Biomedical Engineering, Tohoku University.

解説

MEMS技術を利用した低侵襲医療・ヘルスケア機器の開発

Development of Minimally Invasive Medical Devices and Healthcare Devices Using MEMS Technology

芳賀 洋一
Yoichi HAGA

☆1992年東北大学医学部卒業，1994～1996年東北厚生年金病院勤務，1996年東北大学大学院工学研究科助手，2003年講師，2004年東北大学先進医工学研究機構（TUBERO）助教授，2008年より現職
☆研究・専門テーマは，マイクロ/ナノテクノロジーを用いた医療・ヘルスケア機器の研究・開発
☆正員，東北大学教授 大学院医工学研究科
（〒980-8579 仙台市青葉区荒巻字青葉6-6）
E-mail：haga@bme.tohoku.ac.jp)

松永 忠雄
Tadao MATSUNAGA

☆1994年佐賀大学理工学部電気工学科卒業，同年曙ブレーキ工業（株）入社，2002年東北大学大学院工学研究科学位取得，博士（工学），2004年東北大学先進医工学研究機構助手（のちに，助教）を経て，2010年より現職
☆研究・専門テーマは，MEMSプロセス，医療・福祉用MEMSデバイス
☆東北大学助教 マイクロシステム融合研究開発センター
（〒980-8579 仙台市青葉区荒巻字青葉6-6）
E-mail：matsunaga@bme.tohoku.ac.jp)

1. はじめに

精密な微細加工技術，とくにマイクロマシニング技術やMEMS（微小電気機械システム）技術などを用いることで，今までにない高機能・多機能な医療ツールが実現できる．その用途は大きく以下の四つに分けることができる．

(1) サンプルを体外に取り出した検査機器（μ-TAS，バイオチップ，DNAチップなど）
(2) 低侵襲医療機器（内視鏡，カテーテルなど）
(3) 体内埋込み機器（神経電極，人工網膜など）
(4) ヘルスケア（健康管理）機器

ここでは，人体に直接作用し，計測や治療を行う「身の回りのマイクロ・ナノ」機器として，(2)，(3)，(4)の機器の開発動向と今後求められる技術，そして展望について述べさせていただく．

2. 低侵襲医療機器

低侵襲医療とは，体を大きく切開せずに内視鏡や，医療用チューブ（カテーテル）などを体内に挿入して従来の手術に匹敵する検査や治療を行うもので，患者の身体的，精神的負担を減らせるほか，入院期間を短縮し医療費の削減にも役立つ．内視鏡には主に胃や腸など消化管に用いられる柔らかく屈曲可能な軟性鏡と，腹腔鏡手術や定位脳手術に用いられる棒状の硬性鏡がある．カテーテルは外径数百μm～数mm程度のポリマ製チューブで，血管内などに挿入して用いられる．内視鏡を用いた治療として体内局所の癌，ポリープの摘出や胆嚢摘出術，カテーテルを用いた血管内治療として血管狭窄部を内側から広げることや脳動脈瘤に詰め物をして破裂を防ぐことなどが行われる．

低侵襲医療の新しい流れとして，腹腔鏡治療などにおいて，従来は皮膚に複数の孔を開けて複数の器具を挿入していたのに対し，共通の一つの孔を用いて複数の器具を挿入するSingle Port Access（SPA）Surgeryや，鼻腔から挿入する経鼻内視鏡，軟性内視鏡を用い胃壁や子宮壁を通り抜けて腹腔内臓器の治療までも行うNOTES（Natural Orifice Transluminal Endoscopic Surgery）などが広く行われてきており，血管内カテーテルでは，高周波アブレーションカテーテルによる心腔内からの不整脈治療などがある．

これらに用いられる内視鏡やカテーテルは，より細く小さく，精度よく，安全かつ確実に検査と治療が行えることが求められている．さまざまな利点の一方で，視野が狭い，操作性が劣る，術者の習熟に時間がかかるなどの欠点もある．さらに低侵襲医療の新しい手法や治療対象の広がりに伴い，術者の習熟が追いつかないなどの問題も出てきている．

このような問題を工学技術により解決する試みがいくつかなされている．たとえば硬性鏡の操作をロボット化したロボット外科手術や，飲み込むことで体内の映像をワイヤレスで体外に送信するカプセル内視鏡がある．ロボット外科手術は体内に挿入するツール内のワイヤを体外の電動モータで牽引し鉗子などを動かすシステムであり，これを軟性内視鏡やカテーテルのような多機能化，細径化とともにシャフトの柔軟性が求められる医療ツールにそのまま適用することは難しい．また，システムが大がかりになる欠点もある．飲み込むと消化管内壁の映像をワイヤレスで体外へ送信するカプセル内視鏡は小腸など従来の内視鏡が到達しにくい場所を患者の負担なく観察できる点で有用であるが，体内におけるカプセルの移動や位置合わせの制御は

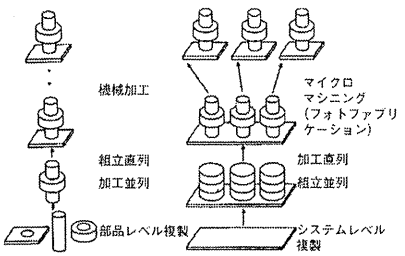

図1 従来の機械加工・組立（左）とフォトファブリケーションによる一括作製（右）

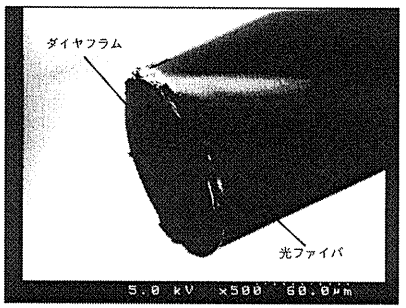

図2 極細径光ファイバ圧力センサ（外径125 μm）

難しく，現状では一般に行われている生検（バイオプシー）や治療には適さない．また，消化管以外，たとえば血管内でカプセル形状のワイヤレスシステムを用いるには，安全に回収または体内で代謝・分解される必要や，移動の制御，小型化に伴うエネルギー供給の問題などを考慮しなければならない．

このような課題を解決するのに，マイクロマシニング，MEMSなどの微細加工技術と新しい材料技術が役立つ．図1のようにウェーハレベルで複雑な機械要素を一括に作製可能で量産性に優れたMEMS技術は，血液や体液を介した感染を防ぐための使い捨て（ディスポーザブル）にも役立つ．今後これらの技術を駆使することにより患者の負担を減らせるばかりでなく，今まで到達が不可能だった部位での検査・治療が可能になるほか，今までにない精密で複雑な検査・治療が可能となる．とくに，マイクロセンサやマイクロアクチュエータを利用することで内視鏡やカテーテルの先で細胞レベル，さらには分子レベルの検査，治療が実現できるようになると期待される．

ピエゾ抵抗効果を利用した半導体ストレンゲージを用いて，体内で用いる医療用のマイクロ力センサや触覚センサ[1]，圧力センサ[2]が試作開発されている．センサはMEMS技術を用いてシリコン基板上に作製される．一方，光ファイバ先端に外力によってたわむ片持ち梁やダイヤフラムを取り付け，外力によるその変位を光学的に読み取ることで，体内に挿入できる細径の圧力センサや力センサになる．図2に直径125 μmの極細径光ファイバ圧力センサを示す[3]．MEMS技術により作製された厚さ0.7 μmの薄いシリコン酸化膜ダイヤフラムが直径125 μmの光ファイバ端面に形成されており，圧力によるダイヤフラムのたわみを白色光の干渉スペクトル変化で検出する．髪の毛程度に細いので，従来のセンサでは挿入不可能な血管内狭窄部や細血管など狭い部位に挿入でき，精密な局所圧測定を行うことができる．センサ構造体はMEMSプロセスを用いてシリコン基板上に多数のダイヤフラム構造を一括で作製し，その後，反応性イオンエッチング（RIE）で貫通エッチングを行い，ダイヤフラムを持った多数の円柱形状パーツを一括作製する．これをガラスキャピラリ内で光ファイバ端面に金属層を介して円柱パーツを接合した後，シリコン円柱部を選択的にエッチング除去する．センサ部が小さいので1回のプロセスで1枚のシリコンウェーハから数十万個という膨大な数のダイヤフラム構造体を得ることができる．

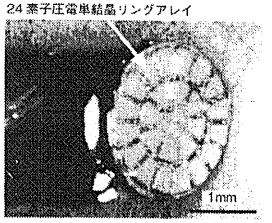

図3 血管内前方視超音波内視鏡（外径2.5mm）

超音波検査法は，体内組織からの超音波反射エコーを利用して体内の構造を可視化する方法で，超音波プローブを小さくすることで体内に持ち込むことが可能になり，体外から観察するよりも精密な画像を得ることができる．内視鏡先端に超音波プローブを搭載したものやカテーテルに搭載され血管内で用いる超音波内視鏡が広く臨床に用いられている．カテーテル進行方向の血管壁と病的な狭窄部を超音波イメージングにより三次元的な可視化を行い，血管内治療を安全かつ確実に行うことを目指し，図3に示すような直径3mmのカテーテル先端搭載用前方視超音波プローブを開発している[4]．微小な振動子でも高い超音波強度，高感度を実現するためPZTよりも圧電特性に優れる圧電単結晶のPMN-PTを超音波振動子として用い微細加工したもので，これをカテーテル端面上に円周状に24個並べ，それぞれが超音波の送信と受信を行う．そのほか，超音波トランスデューサとして，機能性材料を使わずに静電駆動により超音波トランスデューサとなる量産性に適したCMUTsなども医療用応用向けに開発され，血管内超音波内視鏡としての試作も試みられている[5]．また，内視鏡やカテーテル先端から集束した超音波を組織に照射し，病変組織に働きかけ治療する試みもなされている[6]．

一般に，胃カメラなど消化管検査などに用いられる軟性内視鏡の屈曲や，組織をつかむ鉗子の動作は，シャフトを通したワイヤを体外から牽引することで行っており，これは内視鏡手術ツールをロボット化したロボット外科手術でも同様である．ワイヤ牽引を用いた駆動は，ツールを細く小さくする程シャフトが変形しやすくなるため先端の精密

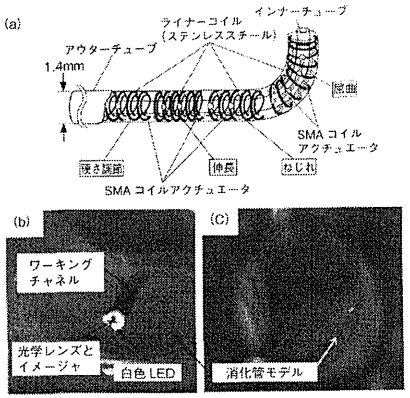

図 4 能動屈曲電子内視鏡 (外径 3.9mm)
(a) 形状記憶合金を用いた能動カテーテルの構成図
(b) 多方向能動屈曲電子内視鏡を腸モデル内に挿入した様子
(c) 先端のイメージャから腸モデルを撮像した様子

な動作ができなくなる．とくに曲がりくねった先では自在な操作はできない．低侵襲医療ツールにマイクロアクチュエータを組み込むことができれば，細く柔らかい機器の先で精密な動作が可能になる．ワイヤに代わる医療用マイクロアクチュエータとして，比較的大きな変位と力が出せる形状記憶合金（SMA），ポリマアクチュエータなどが提案されている．たとえば SMA をカテーテルや内視鏡など医療ツールの先端部に搭載することで，**図 4** のように屈曲，ねじれ回転や伸縮などさまざまな動きを実現できる[7]．具体的な用途としてたとえば，腸の通過障害である腸閉塞の際に腸内容を吸引して減圧治療を行うポリマチューブ先端に屈曲機構を搭載し，病変部に容易に到達できるようにした屈曲チューブなどがある[7]．SMA を用いて多方向に曲がることができる能動屈曲機構先端に CCD や CMOS イメージャを搭載した能動屈曲電子内視鏡は，体内の奥深くに容易に到達し，必要に応じチューブ内腔を通して生検や治療が行えるほか，屈曲機構を低コスト化できるので使い捨て化も可能と期待される[8]．有線は一時的な挿入であればエネルギー供給や回収が容易で，チューブの壁中にスイッチング回路を分布させることで配線数の増加を低減した多関節化や多機能化もできる[9]．

体内に挿入または留置する医療機器の多くは穿刺針や内視鏡の鉗子口を通して体内に挿入されることから一般に円筒形状をしており，半導体微細加工技術など平面基板をベースに発展してきた MEMS 技術がそのまま適応できない場合が多い．とくにカテーテルなど低侵襲医療ツールの多くは貫通穴を持ち，血管造影剤や薬剤の注入，ガイドワイヤなどさらに細い医療ツール挿入のために必要なことから，パーツをカテーテル内腔に配置して貫通穴の機能をなくすことは望ましくない．円筒形状の体内埋込みデバイス，カプセル内視鏡においても，従来の MEMS 技術をそのまま適応すると内腔を有効に利用できない．

図 5 のように電気配線やパッドを形成したフレキシブル基板をらせん形状に巻くことで内腔の確保と柔軟性を実現できるが，基板の厚さや曲率の制限，巻き付けた際の基板端同士のアライメント誤差に気をつける必要がある．図では熱可塑性樹脂である液晶ポリマーを基板材料として用い形状保持を容易にし，はんだバンプを形成した集積回路（ダミー）の実装も行った．回路を巻き付け可能に柔軟にする方法として，プラスチックフィルム上に有機トランジスタを形成し，感圧導電性ゴムと組み合わせカテーテルへらせん形状に巻き付け分布型圧力センサとした例もある[10]．円筒形状の医療ツールに直接微細加工を行う試みがいくつか行われており，たとえばカテーテルの外壁に銅めっきを施しレーザアブレーションを用いて複数の螺旋配線を形成した例がある[11]．筆者らは多方向に屈曲する SMA アクチュエータ作製のために形状記憶済み Ti-Ni 合金製 SMA チューブのフェムト秒レーザ加工を試み[12]，またチューブに転動露光を利用したフォトリソグラフィーと電解エッチングを行い，三つのジグザグばね構造を有した SMA マイクロアクチュエータを試作した[13]．さらに非平面へ MEMS プロセスを適用し，直径 2mm～3mm のガラスチューブ上にレーザ照射を利用したマスクレスフォトリソグラフィーを行い金属ソレノイドコイルパターンや絶縁層を介した多層金属パターンを試作した[14]．これを用いて直径 2mm の MRI（磁気共鳴イメージング）受信コイルをカテーテル先端付近に搭載した体腔内 MRI プローブを開発した例を**図 6** に示す[15]．従来の MRI では体外の励起コイルにより組織から発生する核磁気共鳴（NMR）信号を体外の受信コイルによって受信し像が形成される．たとえば血管内に小型受信コイルを挿入し，撮像対象の近くで受信することで信号強度と S/N 比が向上し**図 6 (b)** のように高解像度のイメージングができる．これにより動脈硬化や粥状硬化，動脈瘤などの病変をより精密に観察，診断できると期待される．コイルはポリイミドチューブ表面の円筒面上へフォトレジストのパターニングと，レジストを型にした銅の電解めっきを用いて作製される．さらに絶縁層を形成し同様の配線形成プロセスを繰り返すことでコイルを多層化でき性能を向上できる（**図 6 (c)**）．NMR 信号の受信と体外への伝送を効率よく行うためにコイル近くに回路を搭載するが，コイル周辺の組織によって最適な共振周波数，インピーダンスが僅かに変動することから，外部からの電圧コントロールにより容量を可変できる集積回路をカテーテルに搭載できるよう小型に設計，試作している．

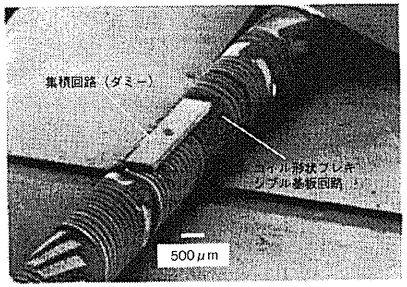

図 5 コイル形状のフレキシブル基板と電子パーツの搭載

3. 体内埋込み機器

体内に留置して神経刺激を行う体内埋込みデバイスとして心臓ペースメーカや人工内耳がすでに広く普及しているが，脳神経との電気的インタフェースを行うための体内埋込みデバイスとして神経束からの信号導出システムおよび神経刺激電極が MEMS 技術を用いて開発されている[16]．また，網膜色素変性症など網膜病変により失明した患者に対して網膜刺激型人工視覚デバイスが[17]，事故による神経の切断などで動かなくなった筋肉に対してワイヤレスで筋肉に電気信号を与えて動かす体内埋込み型電気刺激装置[18]が，それぞれ開発されている．

体内埋込み型の DDS（薬物送達システム）デバイスは，一般に埋込み後の薬剤放出の精密なコントロールや薬の種類の切り換えは難しい．MEMS 技術を利用して体外からワイヤレスで電気的に薬剤放出をコントロールできる埋込み型 DDS デバイスが開発されている．シリコン基板をエッチングして作られた複数の微小ウェルの中に薬剤が封入されており，ウェルをふさぐ蓋を，通電による抵抗加熱または電気分解によって個別に破壊することにより薬剤放出のタイミングと量をコントロールする[19]．

埋込みデバイスとして胸腹部動脈瘤手術中に体内に留置し，術後の血管内局所血圧モニタする小型圧力センサをアメリカ Cardiomems 社などが開発しており，高周波を用いて体外からワイヤレスで給電と信号読み出しを行う．埋込まれるセンサのサイズはたとえば 30mm × 5mm で厚さ 1.5mm 程度となっている[20]．

4. ヘルスケア（健康管理）機器

健康への社会的関心の高まりに伴い，ヘルスケア（健康管理）分野への MEMS 応用の期待が増している．MEMS 技術を用いることで新たな計測が可能になるばかりでなく，デバイスを小さく軽くでき，体表や衣服に常に身に着けるウェアラブル機器としての時間や場所にしばられない生体情報モニタリングが期待される．MEMS を用いたウェアラブルセンサの実例として，アメリカンフットボールプレイヤーのヘルメット内に加速度センサを複数個搭載し，頭部への衝撃をセンシングすることで失神の検知やけかの予防に役立てることが行われており[21]，けがをしたスポーツ選手がリハビリテーションを行う際に呼吸，心拍数，体温や血圧などをモニタし運動量と訓練内容を最適化する試みもなされている[22]．

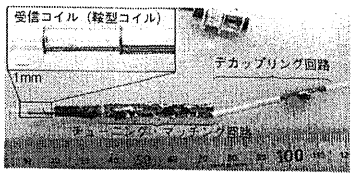

(a) MRI プローブ（外径 2mm の 1 層サドルコイル）

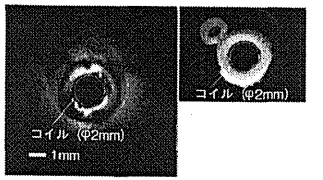

(b) 摘出血管（右）と撮像結果（左）（ブタ鎖骨下動脈）

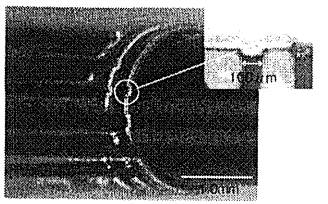

(c) 多層コイル

図 6 体腔内 MRI プローブ

最近の前方視血管内超音波内視鏡の作製技術を応用し，超音波トランスデューサ素子が二次元アレイ状に並んだシート形状のウェアラブル血圧センサを開発した[23]．一般に血圧を測る際は腕や手首などにマンシェットを巻き付けて圧迫するカフ圧迫法が用いられるが，使用者に計測を意識させることなく間欠的に血圧をモニタリングすることは難しい．皮膚上に置いた超音波トランスデューサからパルス波を出し皮下の血管の前壁と後壁の反射エコーを利用し，その遅れ時間を計測することで，血管壁を一定の硬さを持つ管と想定し血管径の変化を計算し，間接的に血圧を測定できる．素子を二次元アレイ状に配置し，ちょうど血管の上に位置し血管径の変化がみられる素子からの信号のみを利用することで皮膚上の超音波トランスデューサ素子と皮下の血管の位置合わせの問題を解決している．**図 7** に装置構成と結果を示すが，手首近くの橈骨動脈において血管内圧の変化と同様の波形が得られている．実使用の際は装着時に従来の血圧測定法を用いて校正を行う．微細加工技術を用いることで薄く軽い超音波トランスデューサアレイシートが実現できる．皮膚上に貼付するデバイスとして，伸縮伸基板材料に電子デバイスを形成することも試みられており，今後の応用展開が期待される[24]．

乳酸や血糖，ストレス物質など生体成分を採血せずモニタリングすることを目指して，皮膚に微小な針を刺し，微小透析（マイクロダイアリシス）を行い，皮下組織液に含まれる生体成分を経皮的に取り出し計測することを行っている．**図 8** は直径約 200 μm の細径金属針の外壁にポリマー（ポリイミド）層による微小流路を形成したもので，流路上のフタのうち皮下に位置する部分に貫通穴を設け，流路に液を循環させる．作製は電着，レーザアブレーション，電解めっきによる犠牲層作製などを用いて行う．マウスの皮下に挿入，留置し，血中の乳酸値と皮下間取液中乳酸の相関が確認できた．乳酸の計測は運動強度の定量化などに役立つ[25]．円皮針と呼ばれる針の付いた絆創膏を皮膚に貼付し継続的な経穴刺激を行う構成にならって，将来，絆創膏上にマイクロポンプと微小透析用タンク，ワイヤレス通信機能を組み合わせ，採血に頼らないウェアラブルな生体成分モニタ装置を目指している．

これらウェアラブルヘルスケア機器は今後，携帯電話やスマートフォンなどを経由してネットワーク上でデータの

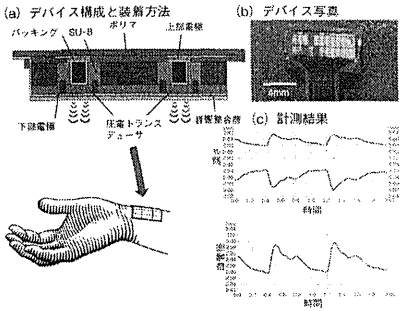

図7　超音波血管径計測によるウェアラブル血圧センサシート

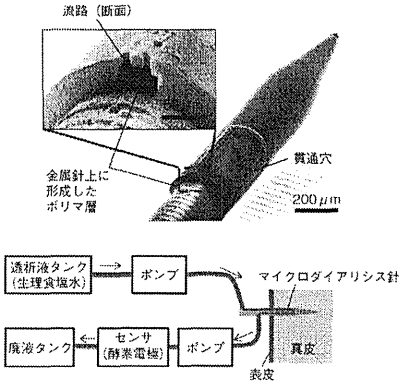

図8　生体成分計測用微小流路を形成した金属針

蓄積や分析を行い，ユーザや医療従事者への有用なフィードバックを行うようになると期待されている[27]．

5. おわりに

低侵襲医療機器，体内埋込み機器など人体に対して用いられる医療機器開発には独特の状況や要求が伴う．具体的には，感染を防ぐための消毒およびディスポーザブル（使い捨て）化の要求，市販前の安全性確認と医療機器としての許認可，臨床医師がユーザーとして手技を行うこと，さらに特殊な販路などがある．また，開発側からみると，少量多品種，ディスポーザブル化による消費量の多さ，効果が高ければデバイスの単価が比較的高く設定できる場合がある，といったマイクロマシン/MEMS技術と合致した利点がある一方，医療機器としての安全性の確保や許認可に費用と時間がかかるリスクが，大きな足かせとなっている．MEMS作製に用いられる高額でランニングコストのかかる製造設備を導入し長期にわたる開発とその後の製造を行うことは一般の医療機器メーカには難しく，実用化のためには製造プロセスの一部を請け負うファウンダリーの活用や，その他さまざまな工夫や新たな仕組み作りが構造や作製上の工夫に併せて求められる．一方で，微細加工技術が提供できる高い信頼性，高機能性は今後の医療に不可欠であり，さまざまな障害はあるものの，微細加工技術分野における今後の技術的進歩と，患者および医療従事者の要望に支えられ，今後いっそう，新たな医療機器の開発が行われていくと期待される．

（原稿受付　2012年11月7日）

●文　献
(1) Takizawa, H. ほか, Development of a Microfine Active Bending Catheter Equipped with MIF Tactile Sensors, *Tech. Digest MEMS'99* (1999), 412.
(2) Kalvesten, E. ほか, The first surface micromachined pressure sensor for cardiovascular pressure measurements, *Tech. Digest MEMS'98*, (1998), 574.
(3) Katsumata, T. ほか, Micromachined 125μm Diameter Ultra Miniature Fiber-Optic Pressure Sensor for Catheter, *Trans. IEE of Japan*, **120-E-2** (2000), 58.
(4) 藤巻慎 ほか, 血管内低侵襲治療のための前方視超音波イメージャーの開発, 生体医工学, **43-4** (2005), 553.
(5) Yeh, D. T. ほか, 3-D Ultrasound Imaging Using a Forward-Looking CMUT Ring Array for Intravascular/Intracardiac Applications, *IEEE Trans. Ultrason. Ferroelectr. Freq. Control*, **53** (2006), 1202.
(6) 安居晃啓 ほか, 小型収束超音波トランスデューサを用いた内視鏡的治療デバイス, 電気学会論文誌 E, **127-2** (2007), 69.
(7) 芳賀洋一 ほか, 屈曲，ねじれ，伸長能動カテーテルの電気めっきによる組み立て, 電気学会論文誌 E, **120-11** (2000), 515.
(8) 水島昌堆 ほか, 形状記憶合金を用いた腫瘤凝固療用能動カテーテル, 日本コンピュータ外科学会誌, **5** (2004), 23.
(9) 牧志 渉 ほか, 使い捨て化と細径化を目指した形状記憶合金を用いた能動屈曲電子内視鏡の開発, 電気学会論文誌 E, **131-3** (2011), 102.
(10) Park, K. ほか, A Multilink Active Catheter with Polyimide-Based Integrated CMOS Interface Circuits, *J. Microelectromech. Syst.*, **8-4** (1999), 349.
(11) Sekitani, T. ほか, Flexible Organic Transistors and Circuits with Extreme Bending Stability, Nature Materials, **9** (2010), 1015.
(12) 三澤 裕 ほか, マイクロカテーテル微細加工技術, 国際マイクロマシンシンポジウム, (1995-11), 123.
(13) Haga, Y. ほか, Medical and Welfare Applications of Shape Memory Alloy Microcoil Actuators, *Smart Mater. Struct.*, **14-5** (2005), 266.
(14) 峯田 貴 ほか, 非平面フォトファブリケーションによる形状記憶合金パイプからのアクチュエータ作製, 電気学会論文誌 E, **123-5** (2003), 158.
(15) Goto, S. ほか, Photolithography on Cylindrical Substrates for Realization of High-Functional Tube-Shaped Micro-Tools, *Proc. Sens. Symp. Sens. Micromachines Appl. Syst.*, (2005-10), 112.
(16) 五島彰二 ほか, カテーテル実装に適した血管内 MRI プローブの開発, 電気学会論文誌 E, **128-10** (2008), 389.
(17) Wise, K. D. ほか, Wireless Implantable Microsystems : High-Density Electronic Interfaces to the Nervous System, *Proc. IEEE*, **92-1** (2004), 76.
(18) Schwarz, M ほか, Single chip CMOS imagers and flexible microelectronic stimulators for a retina implant system, *Sens. Act.*, **A 83** (2000), 40.
(19) Loeb, G. E. ほか, Design and Fabrication of Hermetic Microelectronic Implants, *Proc. IEEE-EMBS Special Topic Conf. on Microtech. in Med. and Biol.* (2000-10), 455.
(20) LaVan, D. A. ほか, Small-scale systems for in vivo drug delivery, *Nature Biotechnology*, **21** (2003), 1184.
(21) Allen, M. G., Micromachined Endovascularly-implantable Wireless Aneurysm Pressure Sensors : from Concept to Clinic, *Proc. Int. Conf. Solid-State Sensors and Actuators (Transducers '05)*, (2005-6), 275.
(22) Jones, W. D. ほか, Helmets Sense The Hard Knocks, *IEEE Spectrum*, (2007-10), 8.
(23) Glaros, C. ほか, A Wearable Intelligent System for Monitoring Health Condition and Rehabilitation of Running Athletes, *Proc. IEEE Conf. on Information Technology Applications in Biomedicine*, (2003), 276.
(24) 鈴木大地 ほか, 超音波計測を用いたウェアラブル血圧センサの開発, 第51回日本生体医工学会大会, (2012-5).
(25) Kim, D. H. ほか, Epidermal Electronics, *Science*, **333** (2011), 838.
(26) Tsuruoka, N. ほか, Development of Minimally Invasive Microdialysis Needle for Continuous Monitoring of Biological Substances, *Tech. Digest MEMS 2012*, (2012-1), 941.
(27) 小谷卓也 ほか, つながる健康機器に電機が集まる, 日経エレクトロニクス, **955** (2007-7), 47.

Remote Fourier transform-infrared spectral imaging system with hollow-optical fiber bundle

Chenhui Huang,[1] Saiko Kino,[1] Takashi Katagiri,[2] and Yuji Matsuura[1,*]

[1]Graduate School of Biomedical Engineering, Tohoku University, 6-6-05 Aoba, Sendai 980-8579, Japan

[2]Graduate School of Engineering, Tohoku University, 6-6-05 Aoba, Sendai 980-8579, Japan

*Corresponding author: yuji@ecei.tohoku.ac.jp

Received 19 June 2012; accepted 28 August 2012;
posted 5 September 2012 (Doc. ID 170882); published 2 October 2012

A spectral imaging system consisting of a Fourier transform-infrared spectrometer, a high-speed infrared camera, and a bundle of hollow-optical fibers transmitting infrared radiation images was constructed. Infrared transmission spectra were obtained by carefully processing multiple interferograms taken by high-speed photography. Infrared spectral images of a variety of samples captured by the system were measured. We successfully detected existence maps of the oil and fat of biological samples by mapping the transmission of specific wavelengths in the spectrum. © 2012 Optical Society of America

OCIS codes: 060.2350, 170.3880.

1. Introduction

Many reports have revealed that malignant tissue can be detected by analyzing absorption spectra because of differences in the protein structures between malignant and normal tissue [1–4]. Fourier transform-infrared (FT-IR) imaging systems with a multichannel detector have been developed to rapidly collect spectra from multiple points on a sample [5]. In addition, infrared spectral imaging systems based on two-dimensional mapping of spectra [6,7] has resulted in highly reliable detection of early tumors [8] and other diseases, and quantitative pathological diagnoses [9] are expected in the future.

Living tissue must be placed inside spectrometers in common measurements with infrared spectral imaging, and only limited parts of the surface of body can be observed *in vivo* [10]. An imaging probe that can be inserted into an endoscope is essential to measure inner organs such as circulatory and digestive systems *in vivo*. However, a common silica-core optical fiber cannot be used due to its extremely strong material absorption in the infrared region. Many types of infrared optical fibers such as chalcogenide glass-core fibers [11] and silver-halide crystalline fibers [12,13] have thus far been developed instead of silica fiber. However, because of the toxicity of the materials or chemical instability, fiber probes made of these materials are not suitable for medical applications. Therefore, we developed a special optical fiber called a hollow-optical fiber [14] for infrared transmission. The structure of the hollow-optical fiber is outlined in Fig. 1. A thin metal film is coated on the inner wall of a polymer or glass capillary. Light is transmitted in the fiber being reflected from the metal film surface, and since the core of the fiber is air, infrared light can be transmitted at low loss without absorption by the material. Furthermore, the hollow-optical fiber is an ideal candidate for application to endoscopes due to its high flexibility and nontoxicity.

To date, we have succeeded in analyzing biomedical samples with single-point measurements using a fiber probe with an optimized attenuated total reflection (ATR) prism [15]. We propose a spectral imaging system based on a hollow-optical fiber bundle [16] that transmits an infrared radiation image to expand the use of the fiber probe to multipoint measurements. We constructed a system consisting of an FT-IR spectrometer, a high-speed infrared camera,

1559-128X/12/296913-04$15.00/0

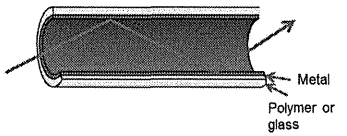

Fig. 1. (Color online) Structure of hollow optical fiber.

and a fiber bundle, so that two-dimensional information from samples could be obtained.

2. Spectral Imaging System

There is a schematic of the measuring system in Fig. 2. The infrared light emitted from the FT-IR spectrometer (Bruker Vertex 70) is focused onto the input end of a hollow-optical fiber bundle by an off-axis parabolic mirror ($f = 50$ mm). The bundle is composed of 19 hollow optical fibers that are 320 μm in inner diameter and 42 cm in length, and the diameter of the bundle is 2.4 mm. The hollow-optical fibers are glass capillaries whose inner walls are coated with a thin silver film and an overcoat of polymer [17] that is transparent in the infrared region. The polymer film is 0.75 μm thick and the fiber has a broad spectrum in the midinfrared range at a low loss level at this thickness. Infrared light emitted from the bundle passes through the sample and is detected by a high-speed infrared camera (FLIR SC-4000) that is composed of a focal plane array (FPA) of InSb. It has 320 × 256 pixels and the detection wavelength ranges from 3 to 5 μm.

There is an example of an interferogram obtained from a single fiber in Fig. 3. The average intensity values of 16 pixels in the fiber core area were computed for all measurements to suppress random noise for a better SN ratio. The interferogram was captured at a frame rate of 1000 fps, and the whole scan took 5.3 s. This means that the frame rate and the processing speed of the camera were high enough to capture a precise interferogram.

The apodization function of $A(x)$ should be applied as indicated in Eq. (1) in Fourier-transform calculations because the working range of the movable mirror in Michelson's interferometer is not infinity:

$$S(v) = \int_0^L A(x)I(x)\cos 2\pi vx\mathrm{d}x. \tag{1}$$

This is where $S(v)$ is the frequency spectrum of light power, $I(x)$ is light intensity at the optical path

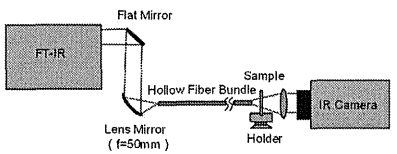

Fig. 2. (Color online) Measurement setup.

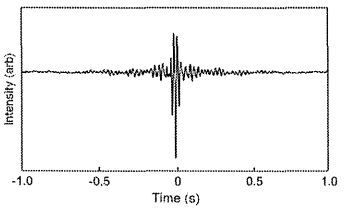

Fig. 3. Interferogram captured with IR camera.

difference of x, and L is the total difference in the optical path. We applied the Happ–Genzel function [18] shown in Eq. (2) by placing emphasis on spectrum resolution:

$$A(x) = 0.54 + 0.46\cos\left(\frac{\pi x}{L}\right). \tag{2}$$

The Fourier-transformed spectra of multiple scans were separately calculated and then averaged to further improve the SN ratio. The infrared camera was synchronized with the FT-IR interferometer by taking a trigger signal from the mirror actuator. The absolute time axis of the interferograms could be obtained due to synchronization and this allowed accurate averaging of multiple interferograms.

Figure 4 shows the power spectra measured at the output end of the fiber. The spectra were Fourier transformations of the interferograms and a spectrum captured by a single-element HgCdTe detector has also been given in the figure for comparison. The absorption peaks in all the spectra at the wavelength of 4.2 μm are of CO_2 in air. Noise and unwanted peak shifts that were seen in the spectrum taken without synchronization are effectively suppressed in the spectrum acquired from the average of 10 interferograms, which were measured by an infrared camera synchronized with FT-IR.

3. Infrared Spectral Imaging

First, the transmission spectra of a polyethylene film were measured to test the capabilities of the system

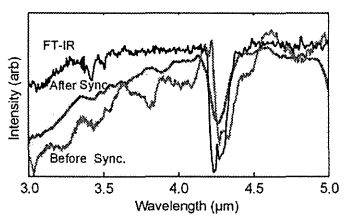

Fig. 4. (Color online) Power spectra measured at output end of fiber.

for infrared spectral imaging. Figure 5 has a transmission spectrum of polyethylene film with a thickness of 35 μm that was measured by using a single hollow-optical fiber and the infrared camera. The absorption peak of a C-H stretched band was confirmed at a wavelength of 3.4 μm.

Second, infrared spectral images were taken while half the output end of the bundle was covered with polyethylene film. The averaged interferogram of nine pixels in the fiber core area of each fiber element was taken in the measurements, and the transmission spectra of all fiber elements were calculated with Fourier transformation. Figure 6 shows the transmittance mapping of 19 fiber elements at the wavelength of 3.4 μm. One can clearly see the border between air and polyethylene film in the image.

We measured transmission images of a mixture of gelatin and oil spread on a glass plate to obtain simulated measurements of biological components. There is a transmission spectrum of the mixture measured with a single hollow fiber in Fig. 7 together with a sample with only gelatin. Strong absorption peaks of C-H stretching in the fatty acid at the wavelength of 3.5 μm were confirmed in the mixture.

Figure 8 shows a transmission spectral image of a sample. Average transmittance in a wavelength range from 3.4 to 3.7 μm is shown in the image and a linear filtering function was applied to smooth the image. This demonstrates the capabilities of the system to obtain absorption mapping of fat and other biological components.

Finally, we tried to obtain a transmission spectral image of a biological sample. We choose a slice of pork as a sample and it was processed into a thin slice with the thickness of 40 μm by using a freezing microtome. The slice was placed on a thin glass plate (150 μm thickness) to obtain infrared transmission images.

Figure 9 shows the transmission spectra of the sliced pork measured in lean and adipose parts. We can see strong absorption peaks of C-H stretching at wavelength of 3.5 μm in the adipose part.

Figure 10 shows a transmission spectral image of a biological sample. The average transmittance in the wavelength range from 3.4 to 3.7 μm is also shown in the image and a linear filtering function was applied to smooth the image. This indicates that the lean and adipose parts in the pork slice could be distinguished by the system and the fiber probe could be applied to the biological tissues.

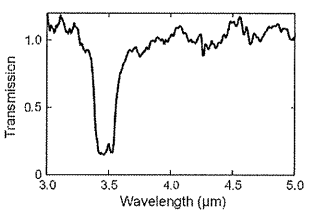

Fig. 5. Transmission spectrum of polyethylene film measured by using single hollow-optical fiber probe.

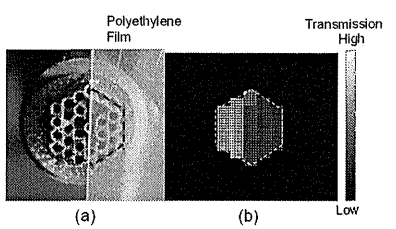

Fig. 6. (Color online) (a) Output end of fiber bundle half covered with polyethylene film. (b) Transmittance mapping of film at wavelength of 3.4 μm.

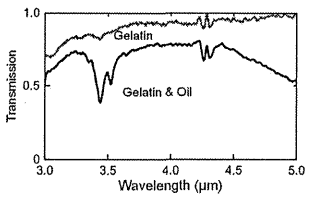

Fig. 7. (Color online) Transmission spectra of mixture of gelatin and oil.

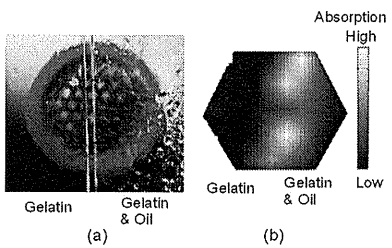

Fig. 8. (Color online) (a) Visible images and (b) transmission spectral images of mixture of gelatin and oil.

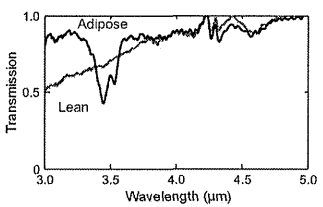

Fig. 9. (Color online) Transmission spectra of lean and adipose pork.

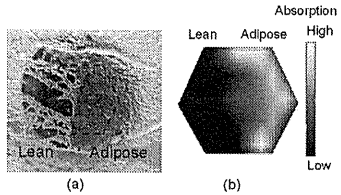

Fig. 10. (Color online) (a) Visible images and (b) transmission spectral images of sliced pork sample.

4. Conclusion

A spectral imaging system based on a bundle of hollow-optical fibers transmitting an infrared radiation image was constructed in this research. The system consisted of an FT-IR spectrometer and a high-speed infrared camera, and infrared transmission spectra were obtained by carefully processing multiple interferograms. We found that infrared spectral images of a variety of samples could be measured with the system. We obtained existence mapping of oil and fat in biological samples by mapping the transmission of specific wavelengths in the spectrum. The number of elements in the bundle in present system is limited because of the diameter of the fiber. Fibers with much smaller diameters are necessary to improve this, although thinner fibers would incur higher losses. We need to discuss other types of fibers that have lower transmission loss even when the core is very small, e.g., hollow-core photonic bandgap fibers [19].

Although transmission images were taken with a fiber bundle in this research, reflection or absorption images are necessary when applying the system to endoscopic diagnosis. However, the reflectance of biomedical tissue is so low that it is difficult to gain sufficient detected power in reflectance measurements. We are therefore developing a microstructured ATR prism that is attached to the distal end of a fiber bundle to measure sample absorption to overcome this difficulty. The details will be reported elsewhere.

References

1. P. Wong, R. Wong, T. Caputo, T. Godwin, and B. Rigas, "Infrared spectroscopy of exfoliated human cervical cells: evidence of extensive structural changes during carcinogenesis," Proc. Natl. Acad. Sci. USA **88**, 10988–10992 (1991).
2. L. McIntosh, M. Jackson, H. Mantsch, M. Stranc, D. Pilavdzic, and A. Crowson, "Infrared spectra of basal cell carcinomas are distinct from non-tumor-bearing skin components," J. Invest. Dermatol. **112**, 951–956 (1999).
3. Y. Xu, L. Yang, Z. Xu, Y. Zhao, X. Ling, Q. Li, J. Wang, N. Zhang, Y. Zhang, and J. Wu, "Distinguishing malignant from normal stomach tissues and its *in vivo*, *in situ* measurement in operating process using FTIR fiber-optic techniques," Sci. China Ser. B **48**, 167–175 (2005).
4. D. Maziak, M. Do, F. Shamji, S. Sundaresan, D. Perkins, and P. Wong, "Fourier-transform infrared spectroscopic study of characteristic molecular structure in cancer cells of esophagus: an exploratory study," Cancer Detect. Prev. **31**, 244–253 (2007).
5. S. Kazarian and K. Chan, "Applications of ATR-FTIR spectroscopic imaging to biomedical samples," Biochim. Biophys. Acta **1758**, 858–867 (2006).
6. P. Garidel and M. Boese, "Mid infrared microspectroscopic mapping and imaging: a bio-analytical tool for spatially and chemically resolved tissue characterization and evaluation of drug permeation within tissues," Microsc. Res. Tech. **70**, 336–349 (2007).
7. R. Mendelsohn, M. Rerek, and D. Moore, "Infrared spectroscopy and microscopic imaging of stratum corneum models and skin," Phys. Chem. Chem. Phys. **2**, 4651–4657 (2000).
8. J. Anastassopoulou, E. Boukaki, C. Conti, P. Ferraris, E. Giorgini, C. Rubini, S. Sabbatini, T. Theophanides, and G. Tosi, "Microimaging FT-IR spectroscopy on pathological breast tissues," Vib. Spectrosc. **51**, 270–275 (2009).
9. R. Mendelsohn, E. Paschalis, P. Sherman, and A. Boskey, "IR microscopic imaging of pathological states and fracture healing of bone," Appl. Sectrosc. **54**, 1183–1191 (2000).
10. L. B. Mostaço-Guidolin, L. S. Murakami, A. Nomizo, and L. Bachmann, "Fourier transform infrared spectroscopy of skin cancer cells and tissues," Appl. Spectosc. Rev. **44**, 438–455 (2009).
11. J. Nishii, T. Yamashita, and T. Yamagishi, "Coherent infrared fiber image bundle," Appl. Phys. Lett. **59**, 2639–2641 (1991).
12. I. Paiss and A. Katzir, "Thermal imaging by ordered bundles of silver halide crystalline fibers," Appl. Phys. Lett. **61**, 1384–1386 (1992).
13. Y. Lavi, A. Millo, and A. Katzir, "Thin ordered bundles of infrared-transmitting silver halide fibers," Appl. Phys. Lett. **87**, 241122 (2005).
14. Y. Matsuura, M. Saito, M. Miyagi, and A. Hongo, "Loss characteristics of circular hollow wave guide for incoherent infrared light," J. Opt. Soc. Am. A **6**, 423–427 (1989).
15. Y. Matsuura, S. Kino, and T. Katagiri, "Hollow-fiber-based flexible probe for remote measurement of infrared attenuated total refection," Appl. Opt. **48**, 5396–5400 (2009).
16. Y. Matsuura and K. Naito, "Flexible hollow optical fiber bundle for infrared thermal image," Biomed. Opt. Express **2**, 65–70 (2011).
17. Y. Abe, Y. Shi, Y. Matsuura, and Miyagi, "Flexible small-core hollow fibers with an inner polymer coating," Opt. Lett. **25**, 150–152 (2000).
18. J. F. Rabolt and R. Bellar, "The nature of apodization in Fourier transform spectroscopy," Appl. Spectosc. **35**, 132–135 (1981).
19. F. Benabid, "Hollow-core photonic bandgap fibre: new light guidance for new science and technology," Phil. Trans. R. Soc. A **364**, 3439–3462 (2006).

International Journal of Applied Electromagnetics and Mechanics 39 (2012) 1041–1046
DOI 10.3233/JAE-2012-1576
IOS Press

Haptic perception mechanism of softness

Daisuke Tsuchimi[a,*], Takeshi Okuyama[b] and Mami Tanaka[a]
[a]*Graduate School of Biomedical Engineering, Tohoku University, Sendai, Japan*
[b]*Graduate School of Engineering, Tohoku University, Sendai, Japan*

Abstract. A palpation is convenient and it is a useful method to detect a cancer and to evaluate softness of skin. However, the palpation is skillful method, and the mental/physical conditions of the experts affect the result of the palpation easily. The result of palpation is subjective and it is hard to share the result with the other people. Therefore, the development of the sensor that can measure the softness of the body is demanded. In this paper, a relationship between physical properties of measured objects and the softness that human feel are investigated for a development of a tactile sensor system. At first, the relationship between tactile softness and stiffness of the measured objects is investigated. As a result, tactile softness decreases with the increase of stiffness of the objects. Next, the relationship between tactile softness and size of contact area of human finger are investigated. These results lead to the conclusion that there is a possibility that tactile softness of the objects are not only related to the contact force or displacement of a finger and the objects but also to the contact area of the finger and the measured objects.

Keywords: Tactile, stiffness, softness

1. Introduction

Human skin, which mainly consists of epidermis, dermis and hypodermis, is the largest organ of a human body. It has a lot of roles, for example, protection function, moisture maintenance function and sensory function. Moreover, it becomes a parameter that shows the health and beauty conditions, because the skin is the outermost layer of a human body.

A palpation is convenient and it is a useful method to detect a canter and to evaluate softness of skin. However, the palpation is skillful method. The mental/physical conditions of the experts affect the result of the palpation easily. The result of palpation is subjective and it is hard to be shared with other people. Therefore, the development of the sensor that can measure the tactile softness of the body is demanded [1, 2]. Some sensors for measuring prostate cancer [3] or hardness of human skin [4] are developed, but no sensor meets the requirements.

In this paper, the relationships between physical properties of soft objects and the tactile softness are investigated in order to develop a tactile sensor system. After this, the tactile softness means touch feeling of softness which when human touches an object. First, the relationship between stiffness of measured objects and the tactile softness is investigated using silicone blocks with different Young's modulus. Next, the influence of contact area between the objects and human finger for evaluation of tactile softness are investigated using silicone blocks with different Young's modulus.

*Corresponding author: Daisuke Tsuchimi, Graduate School of Biomedical Engineering, Tohoku University, Aoba 6-6-04, Aramaki, Aoba-ku, Sendai 980–8579, Japan. Tel.: +81 22 795 5879; Fax: +81 22 795 5879; E-mail: d.tsuchimi@rose.mech.tohoku.ac.jp.

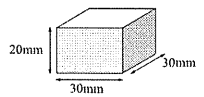

Fig. 1. Dimension of the silicone object.

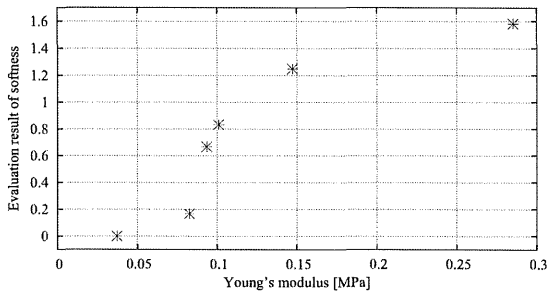

Fig. 2. The result of Scheffé's paired comparison (Nakaya variation).

2. Relationship between stiffness and tactile softness

To investigate the mechanism of evaluating tactile softness of human, the relationship between stiffness of evaluated objects and tactile softness when human touch to the object and feel is investigated. In experiments, six kinds of silicone block objects with different Young's modulus are prepared. Figure 1 shows the prepared measuring objects. The dimensions of these objects are 30 mm width, 30 mm length, and 20 mm thickness. Young's modulus of them are 0.37, 0.82, 0.94, 1.01, 1.47, and 2.86×10^{-1} MPa. Young's modulus of the objects are determined by reference to Young's modulus of epidermis, dermis and hypodermis of skin [5–8].

Using these silicone objects, a sensory test of tactile softness is conducted. In an experiment, two objects are picked out of the six objects, and those are placed on the force sensor. Six subjects touch the objects using their forefinger alternately, and compared tactile softness of two objects. The subjects are 20 to 32 years old men. The force sensor measure the contact force applied on the objects vertically when a subject touch the object. The sensory tests are conducted in total 15 combinations of the six objects. The results of sensory test were evaluated using Scheffé paired comparison method [9].

Figure 2 shows the result of sensory test. Each value in the figure shows difference of tactile softness of subject's score with reference to the object of Young's modulus 0.37×10^{-1} MPa. The higher value indicate that the subjects evaluate the object harder. As the result, the subjects answered the object with high young's modulus is harder in 97% of all trial, and it found that the tactile softness of the objects decrease with increase of Young's modulus of the objects. Young's modulus and stiffness of the objects mean the same tendency, because thickness of all objects are the same. It can be said that tactile softness of the objects are decrease with increase of stiffness of the objects.

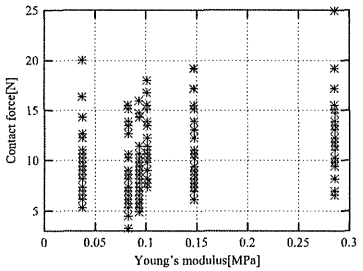

Fig. 3. Contact force applied to each object.

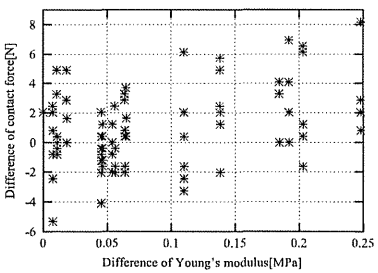

Fig. 4. Differences of the contact force.

Figure 3 shows the contact force applied to the objects by the subjects using their forefinger in the sensory test. The horizontal axis values are Young's modulus of the objects. The contact force is almost 5 to 15 N. And the contact force seem to increases with increase of Young's modulus, but there is no significant difference.

Figure 4 shows the differences of the contact force between the compared two objects. The horizontal axis values are differences of Young's modulus between compared two objects. The vertical axis values are differences of the contact force between compared two objects, and these values calculated to take contact force value with softer object from harder object. Therefore the negative difference values in the figure mean that the subjects touch softer object with higher contact force. This figure shows that the differences of the contact force tend to increase with increase of the differences of Young's modulus. But the differences of the contact force vary widely, and there are some negative value. Therefore, it is difficult to evaluate the tactile softness of the objects with only contact force information.

3. Influence of contact area upon tactile softness evaluation

According to the result of Chapter 2, it is difficult for the subjects to evaluate the tactile softness of the objects with only contact force information. Therefore, the influence of contact area upon perception of tactile softness evaluation is investigated. We consider that the perception of tactile softness is affected by the contact area information in two ways. One is a size of contact area between subjects' finger and evaluated objects. Another is variation of the contact area size in touch motion. And the latter is investigated in this paper.

At first, the relationship between contact force and contact area is investigated. Four panelists push their forefinger into three silicone blocks with ink, in such a way as to evaluate tactile softness of the blocks. The contact force is measured using a pressure sensor, and the size of contact area between the forefinger and the blocks are calculated using ink blot on the blocks. Figure 5 shows the results of the experiment. The size of contact area are normalized using the softest silicone block. As the results, the size of contact area decrease with increase in Young's modulus of the blocks. Thus, the influence of contact area between the finger and an object upon evaluation of tactile softness is investigated through the two kinds of sensory tests with four silicone objects.

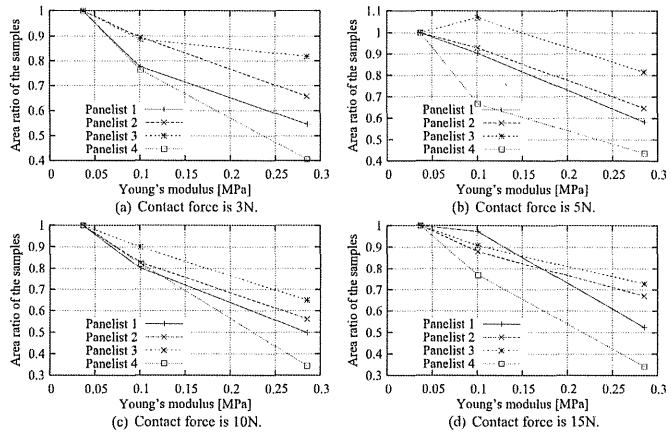

(a) Contact force is 3N. (b) Contact force is 5N.

(c) Contact force is 10N. (d) Contact force is 15N.

Fig. 5. The relationship between contact area and Young's modulus.

Second, four kinds of silicone softness objects are prepared for the sensory tests. Dimensions of these objects are 30 mm width, 30 mm length, and 20 mm thickness. Young's modulus of the objects in the sensory tests are 0.37, 0.83, 1.01, and 1.47×10^{-1} MPa. There were six kinds of Young's modulus in the previous experiment. But, in a preliminary experiment, it was found that it is impossible for the subjects to discriminate the objects that have quite similar Young's modulus using piston device described below. And tactile softness of the object with 2.86×10^{-1} MPa Young's modulus is quite far from the others. Therefore, we have excluded the objects with 0.94×10^{-1} MPa and 2.86×10^{-1} MPa Young's modulus to reduce the subjects' burden.

In the sensory tests, two objects are picked out of the four objects, and named object A and object B. Six subjects touch the objects using their forefinger, and compare tactile softness of the objects. The subjects are 20 to 32 years old men. The sensory tests are conducted in total 6 combinations of the four objects. Table 1 shows the result of the first sensory test. In the table, "s1" to "s6" mean the subjects, and the item of "A" or "B" in "Evaluation of subjects" means the object that the subject evaluated harder. Almost all subjects evaluate that the object with higher Young's modulus is harder.

Next, the subjects evaluate the tactile softness of the objects through the cylinder piston device as shown in Fig. 6.

The cylinder piston device consists a of piston, and a stage. Shapes of the contact 1 is 5 mm square. And that of the contact 2 is 10 mm square. The size of contact 1 is sufficiently-small as compared with the contact area between their forefinger and the objects in the first sensory test. The piston moves vertically in accordance with the motion of a subject's forefinger. The subject pushed the objects using the device to evaluate the tactile softness of the objects. The size of contact area between their forefinger and contact 1 is constant, and the subjects forced to evaluate tactile softness of the object without influence of contact area information. The results of the experiments are evaluated using Scheffé paired comparison

Table 1
The result of the first sensory test of tactile softness

Young's modulus [MPa]		Evaluation of subjects					
Object A	Object B	s1	s2	s3	s4	s5	s6
0.147	0.101	A	A	A	A	A	A
0.147	0.083	A	A	A	A	A	A
0.147	0.037	A	A	A	A	A	A
0.101	0.083	A	A	A	A	A	A
0.101	0.037	A	A	A	A	A	A
0.083	0.037	B	A	A	A	A	A

Table 2
The result of the second sensory test of tactile softness using cylinder piston device

Young's modulus [MPa]		Evaluation of subjects					
Object A	Object B	s1	s2	s3	s4	s5	s6
0.147	0.101	A	A	A	A	A	B
0.147	0.083	A	A	A	A	A	A
0.147	0.037	A	A	A	A	A	A
0.101	0.083	A	A	B	A	A	A
0.101	0.037	A	B	A	A	A	A
0.083	0.037	B	A	A	A	A	B

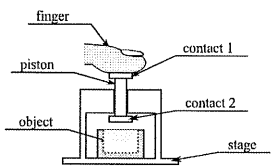

Fig. 6. A cylinder piston device for sensory test.

method. After that, the subjects are asked about the difficulty of the evaluation in the first sensory test and the second sensory test.

Table 2 shows the result in the second sensory test. "Evaluation of subjects" means the object that the subject evaluated harder. Some subjects tend to evaluate that the object with lower Young's modulus is harder. The percentage of the subjects that evaluated the object with higher Young's modulus as harder in all trials is 97.2% in the first sensory test, but that is 86.1% in the second sensory test. It was confirmed that all subjects feel it difficult to evaluate tactile softness of the objects in the second sensory test than that in the first sensory test. These results show that the contact area information can be needed to compare tactile softness difference between slight different objects.

4. Conclusions

In this paper, the relationship between the stiffness and the tactile softness of a soft objects was confirmed through the sensory test. The result of the sensory test showed that the tactile softness of the objects decrease with increase of stiffness of the objects. The influence of contact area information upon tactile softness evaluation was also investigated through two sensory tests. In the first test, the subjects

evaluated tactile softness of objects using their forefinger. The subjects evaluated tactile softness of the objects through a cylinder piston device in the second test. It was found that the percentage of correctly evaluation decline in the second sensory test. And the contact area information can be needed to evaluate slight difference of tactile softness between the similar objects.

References

[1] J. Jurczyk and K. Loparo, Mathematical transforms and correlation techniques for object recognition using tactile data, robotics and automation, *IEEE Transactions on* 5(3) (1989), 359–362.
[2] A. Eklund, A. Bergh and O. Lindahl, A catheter tactile sensor for measuring hardness of soft tissue: Measurement in a silicone model and in anltigtin vitroltigt; human prostate model, *Medical and Biological Engineering and Computing* **37** (1999), 618–624.
[3] H. Makoto, N. Hirofumi, T. Mami, T. Yoshikatsu and C. Seiji, Development of a active palpation sensor wearable on a finger for detecting prostate cancer and hypertrophy, *JSME Annual Meeting* 2006 (5) (2006), 593–594.
[4] K. Tadashi, S. Hideaki and N. Hajime, Development of a softness sensing system by using dynamic response of piezoelectric vibrator and its application to detect mechanical properties of living cells, *JSME International Journal Series C, Mechanical Systems, Machine Elements and Manufacturing* **43**(4) (2000), 772–779.
[5] Y. Yoshikawa, Mechanical behavior of skin and measurement way (hardness measurement of a living body and artificial judge<special story>), *Measurement and Control* **3**(14) (1975), 263–280.
[6] Y. Kazuo, T. Hidehiko and O. Shotaro, Physical characteristics of human finger, *Biomechanisms* **3** (1975), 27–36.
[7] Y.C. Fung, Biomechanics: Mechanical properties of living tissues, 2nd Edition, Springer, 1993.
[8] T. Maeno, K. Kobayashi and N. Yamazaki, Relationship between the structure of finger tissue and the location of tactile receptors, *Transactions of the Japan Society of Mechanical Engineers* **Series C 63**(607) (1997), 881–888.
[9] N. Sumiko, A transform of scheffeąńs method(japanese), in: *Proceeding of 11th Sensory Test Conference, Union of Japanese Scientists and Engineers*, 1970.